

Quantifying hydrogen bonding using electrically tunable nanoconfined water

Ziwei Wang^{1,2,*}, Anupam Bhattacharya¹, Mehmet Yagmurcukardes³, Vasyly Kravets¹, Pablo Díaz-Núñez^{1,2}, Ciaran Mullan¹, Ivan Timokhin^{1,2}, Takashi Taniguchi⁴, Kenji Watanabe⁴, Alexander N. Grigorenko¹, Francois Peeters⁵, Kostya S. Novoselov^{1,2,6}, Qian Yang^{1,2,*}, Artem Mishchenko^{1,2,*}

¹*Department of Physics and Astronomy, University of Manchester, Manchester M13 9PL, UK.*

²*National Graphene Institute, University of Manchester, Manchester M13 9PL, UK.*

³*Department of Photonics, Izmir Institute of Technology, 35430, Izmir, Turkey*

⁴*National Institute for Materials Science, Tsukuba, Japan*

⁵*Department Physics, University of Antwerp, B-2020 Antwerpen, Belgium*

⁶*Institute for Functional Intelligent Materials, National University of Singapore, Singapore, Singapore*

ziwei.wang@manchester.ac.uk, qian.yang@manchester.ac.uk, artem.mishchenko@manchester.ac.uk

Hydrogen bonding plays a crucial role in biology and technology, yet it remains poorly understood and quantified despite its fundamental importance¹⁻⁶. Traditional models, which describe hydrogen bonds as electrostatic interactions between electropositive hydrogen and electronegative acceptors, fail to quantitatively capture bond strength, directionality, or cooperativity, and cannot predict the properties of complex hydrogen-bonded materials^{2,6-12}. Here, we introduce a novel approach that conceptualizes the effect of hydrogen bonds as elastic dipoles in an electric field, which captures a wide range of hydrogen bonding phenomena in various water systems. Using gypsum, a hydrogen bond heterostructure with two-dimensional structural crystalline water, we calibrate the hydrogen bond strength through an externally applied electric field. We show that our approach quantifies the strength of hydrogen bonds directly from spectroscopic measurements and reproduces a wide range of key properties of confined water reported in the literature. Using only the stretching vibration frequency of confined water, we can predict hydrogen bond strength, local electric field, O-H bond length, and dipole moment. Our work also introduces hydrogen bond heterostructures – a new class of electrically and chemically tunable materials that offer stronger, more directional bonding compared to van der Waals heterostructures, with potential applications in areas such as catalysis, separation, and energy storage¹³⁻¹⁸.

Hydrogen bonds (HBs) are unique intermolecular interactions that are stronger and more directional than weak and isotropic van der Waals forces, yet weaker and less directional than covalent bonds. HBs are typically defined as attractive interactions between a hydrogen atom (H) and an acceptor group (A) in a system represented as D-H...A, where H is covalently bonded to an electronegative donor group (D), while H carries a partial positive charge δ^+ ^{7,8}. A key feature of HBs is their directionality, often with a D-H...A angle close to 180°. In water and similar systems, where distance between D and A is typically greater than 2.5 Å, the electrostatic attraction between H (δ^+) and A (δ^-) is believed to be the primary factor contributing to the strength of HBs^{2,6,9-11}.

HBs could significantly alter the properties of residing system. For instance, the formation of HBs in water has a pronounced impact on the physical properties of its condensed phases – ice. Often, hydrogen-bonded systems form extensive networks of HBs that extend over long ranges and in various directions, as seen in liquid water, ices, hydrogels, proteins, and DNA molecules. The complexity of these networks, along with the presence of interfaces or external electric fields in realistic heterogeneous systems, makes it difficult to analyse them using classic definition of HBs or to predict the properties of such systems¹². To address these challenges, the electrostatic model of HBs, initially proposed decades ago that based on point charge approximation¹⁹, has been refined with various treatments, such as electron distribution calculations²⁰ and orbital hybridization theory²¹, leading to a more sophisticated description of HBs. Despite advancements in modelling and the introduction of spectroscopic methods, which provide direct information on molecular vibrations of hydrogen-

bonded species²², a practical and efficient experimental approach to quantitatively predict the properties of HBs is still lacking.

We propose a new approach that conceptualises an HB as an electric dipole moment \mathbf{p} of the donor-hydrogen (D-H) pair interacting with the electric field \mathbf{E} induced by the acceptor A (**Fig. 1a**). In this model, the dipole moment ($\mathbf{p} = q\mathbf{d}$) arises from the separation of the charge q along the D-H bond direction $\mathbf{d}_{D \rightarrow H}$, while the field \mathbf{E} of A provides electric potential energy $U_{HB} = -\mathbf{p} \cdot \mathbf{E}$. This energy is maximized when the electric field and the dipole are aligned. When subject to external electric field, the projected external electric field (E_{Ext}) along the HB direction effectively alters the spring constant and dipole moment of the electric dipole, thus changing the overall electrostatic interactions of the HBs system. This offers a more universal and precisely quantifiable dipole-in- E -field alternative to the abstract chemical bond definition of HBs. Our model reflects both the dominant electrostatic nature of HBs (electric potential energy U_{HB} as a quantitative measure of HB strength) and their directionality (the angle between \mathbf{p} and \mathbf{E}_{HB} , **Fig. 1b**). Moreover, by treating individual HBs as electric fields exerting on separate dipoles, our method allows the overall properties of a system with complex HB networks to be predicted based on the superposition of dipole moments and electric fields. In this work, we introduce the dipole-in- E -field approximation for HBs and use naturally occurring hydrogen-bonded heterostructure gypsum to quantitatively describe HBs in nanoconfined water.

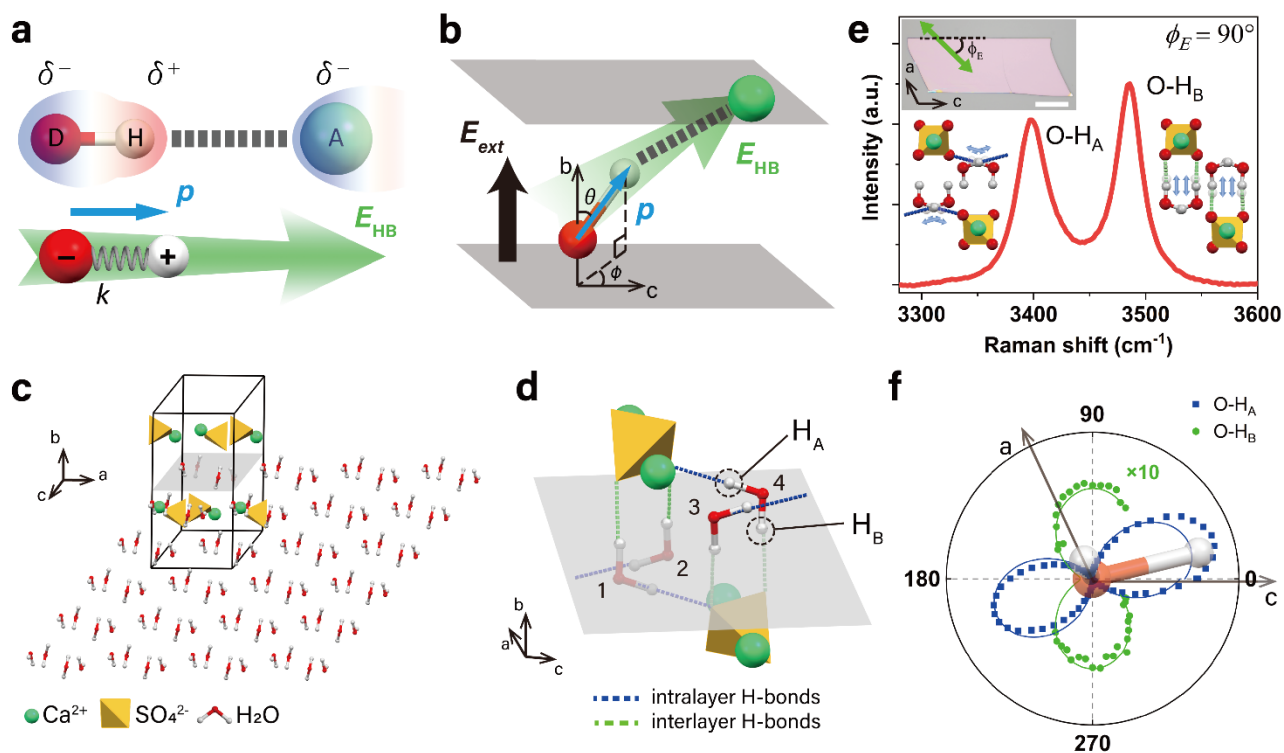


Fig. 1: Hydrogen bond model and gypsum system. **a**, Hydrogen bond models. The upper diagram represents conventional model. Red and green atoms are negatively charged (δ^-) donor (labelled as D) and acceptor (labelled as A), respectively. Hydrogen (H) atom carries partial positive charge (δ^+). The lower diagram represents our dipole-in- E -field approach, where the HB is conceptualised as an electrostatic interaction of a dipole oscillator, with spring constant k and dipole moment \mathbf{p} (blue arrow), in the local field E_{HB} (green arrow) of a negatively charged acceptor. **b**, Schematics of the HB in **a** when subjected to an external electric field (E_{ext}) along the out-of-plane direction. The orientation of the dipole is described by angles θ and ϕ . **c**, Unit cell of gypsum (in the box) and the extended confined water (oxygen in red, hydrogen in white) plane in the same two-dimensional molecular sheet. **d**, Zoomed-in sketch of **c** showing two types of O-H dipoles, intralayer O- H_A and interlayer O- H_B . **e**, Raman spectrum of water stretching modes in an exfoliated thick gypsum crystal, assigned to the stretching of O- H_A and O- H_B dipoles. Schematics of stretching vibrations are shown next to the respective peaks as insets. The

top inset is an optical micrograph of exfoliated thick gypsum flake on a CaF₂ substrate. The polarization of laser is described by ϕ_E , the angle between laser polarization (green arrow) and gypsum crystalline c-axis (dashed line). Scale bar 30 μm . **f**, Angle-resolved Raman intensity of O-H_A (blue squares) and O-H_B stretching (green circles) stretching modes. Solid lines the sinusoidal fittings used to obtain ϕ_A and ϕ_B (ϕ defined in **b**) of water molecules in gypsum. The projection of a water molecule on the gypsum α -c plane is shown in the centre as an inset.

Conventionally, the strength of HBs is characterized as a shift in the stretching vibration frequency of the D-H covalent bond: the stronger the HB, the more red-shifted the frequency ($\omega_{\text{D-H}}$). Here we consider the HB as D-H dipole in the presence of a local electric field, with the red shift in frequency depending on the local field produced by the acceptor (\mathbf{E}_{HB}). In a harmonic first-order approximation, the total potential energy (U_{osc}) and electric potential energy (U_{HB}) of D-H dipole oscillator in E -field are given by:

$$U_{\text{osc}} = \frac{1}{2}k(|\mathbf{x}| - |\mathbf{d}|)^2 + U_{\text{HB}} \quad (1)$$

$$U_{\text{HB}} = -\mathbf{p} \cdot \mathbf{E} + \dots \quad (2)$$

Here, k is the force constant of the D-H bond, \mathbf{d} and \mathbf{x} are vectors pointing from the donor (at rest) to the equilibrium and instantaneous positions of hydrogen, respectively. The \mathbf{E} field changes the equilibrium bond length and bond alignment elastically. In the absence of rotation, the problem is simplified to one dimension, with the vectors \mathbf{d} , \mathbf{x} , and \mathbf{E} reduced to their colinear components along D-H bond (see **Methods**, ‘Full form of the dipole-in- E -field approximation’). Using Hooke’s law, $d(E) = d(0) + F(E)/k(E)$, we can express both the electrostatic force $F(E)$ and the force constant $k(E)$ as derivatives of the potential energy around equilibrium as $F(E) = -\frac{\partial U_{\text{HB}}}{\partial d}$ and $k(E) = -\frac{\partial^2 U_{\text{osc}}}{\partial d^2}$, leading, in a linear approximation, to the E -field dependent equilibrium bond length $d(E)$ and force constant $k(E)$ ²³:

$$d(E) = d(0) + \frac{E}{k(E)} \frac{\partial p}{\partial d} \quad (3)$$

$$k(E) = k(0) - \frac{\partial^2 p}{\partial d^2} E \quad (4)$$

Here, $d(0)$ and $k(0)$ are the equilibrium bond length and the force constant of a free D-H bond in the absence of the HB, respectively. In the harmonic approximation, the force constant $k(E)$ of D-H bond can be determined experimentally (using vibrational spectroscopy) from the stretching vibration frequency $\omega_{\text{D-H}}$ of the D-H bond, $k(E) = \mu\omega_{\text{D-H}}^2$, where μ is the reduced mass of the D-H system. To obtain the coefficient $\partial^2 p/\partial d^2$ in the Eq. 4, we performed vibrational spectroscopy experiments on water HBs in a solid-state system where the rotational degree of freedom of water molecules is suppressed.

We chose gypsum (CaSO₄·2H₂O) as our model system. Gypsum is one of the most abundant minerals on Earth and consists of alternating water bilayers and ionic CaSO₄ sheets^{24,25}. In gypsum, water molecules are confined and orientated between CaSO₄ walls via HBs, forming a two-dimensional (2D) water crystal that extends along the gypsum a - c plane (**Fig. 1c**). We selected gypsum for three main reasons. First, the low dimensional hydrogen bonded water in gypsum offers a favourable platform to study 2D confined water – a hot topic by its nature, and simplifies relevant theoretical analysis. Second, the stretching vibrations of the two O-H dipoles in the gypsum water molecules are sufficiently decoupled. In gypsum, water molecules are arranged in four orientations with two distinct types of HBs, resulting in two groups of O-H dipoles in different crystallographic environments^{25,26}: O-H_A, bonded by a stronger intralayer HB, and O-H_B, with a weaker interlayer HB nearly parallel to the b -axis (**Fig. 1d**). **Figure 1e** shows the Raman spectrum of the H₂O stretching vibrations in a bulk gypsum crystal, with two peaks centred at 3405 cm⁻¹ and 3490 cm⁻¹ attributed to the stretching vibrations of O-H_A and O-H_B bonds, respectively (see details in **Methods**, ‘Decoupling of the stretching frequencies of O-H bonds in crystalline water of gypsum’). The polar plot in **Fig. 1f** shows the angle-resolved Raman intensity of O-H_A and O-H_B modes with respect to the a - c plane of gypsum. The angles of maximal intensity are $\phi_E = 18^\circ$ for O-H_A and $\phi_E = 90^\circ$ for O-H_B, with a difference of 72°. In subsequent experiments, we used these polarizations to obtain maximum O-H stretching signal.

Third, gypsum can be easily exfoliated into few-layer sheets, which are stable in ambient conditions. This enables us to apply van der Waals technology²⁷ to construct gypsum heterostructures, which allows us to apply

external electric field E_{ext} while simultaneously probing the vibrational response of confined water. To this end, we sandwiched gypsum crystals (50-150 nm thickness) between hexagonal boron nitride (hBN) and few-layer graphene (FLG) to form heterostructures (**Fig. 2a,b**), resembling a parallel plate capacitor. The top and bottom FLGs allow us to apply E_{ext} as a perturbation to the local field E_{HB} of the acceptor A (in the case of gypsum, A is the oxygen atom in sulphate group, see **Fig. 1b**). We then measured Raman spectra of these two O-H stretching vibrations with the E_{ext} field applied along the out-of-plane b-axis. The colour maps in **Fig. 2c,d** show the evolution of the Raman spectra for O-H_A and O-H_B stretching vibrations as a function of E_{ext} at 80 K, respectively. Both maps illustrate the impact of E_{ext} on the O-H stretching vibration frequency, with O-H_A showing pronounced peak splitting and O-H_B showing peak shifting. These observed changes are attributed to alterations of the total electric field ($E_{\text{tot}} = E_{\text{HB}} + E_{\text{ext}}$) acting on different types of O-H bonds in gypsum. The inset of **Fig. 2e** demonstrates how E_{tot} differs for O-H dipoles that point towards opposite directions.

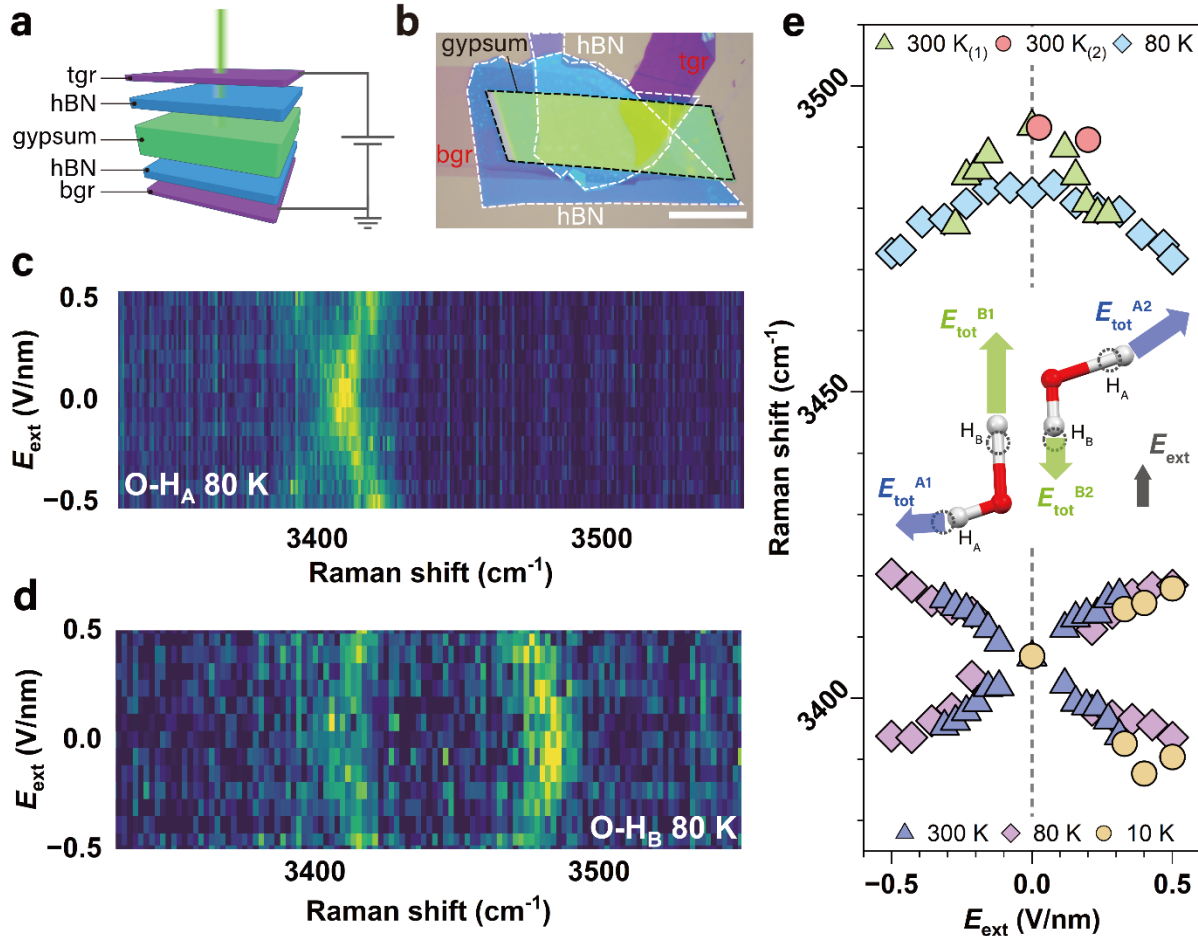


Fig. 2: Electric field effects on O-H dipole stretching vibration. **a**, Schematic of Raman measurements with E_{ext} applied to a tgr/hBN/gypsum/hBN/bgr heterostructure. **b**, Optical micrograph of one of our gypsum heterostructure devices. tgr and bgr refer to top and bottom FLG electrodes. Scale bar is 20 μm. **c-d**, Colour maps of Raman spectra for O-H_A (**c**) and O-H_B (**d**) at 80 K under E_{ext} . Colour from dark blue to yellow indicates increasing Raman intensity. **e**, Raman peak positions of the two O-H stretching modes at different temperatures under E_{ext} . The inset shows the change in O-H dipoles and E_{tot} under E_{ext} , the effect is exaggerated for clarity. Dashed circles mark positions of H atoms in the absence of E_{ext} .

We observed similar behaviour for the O-H_A stretching in Fourier transform infrared (FTIR) spectroscopy measurements at low temperature (**Extended Data Fig. 1**). The observed effects from E_{ext} are reversible within our measurement range of ± 0.5 V/nm, as the spectra revert to their original state when E_{ext} was removed (**Extended Data Fig. 2**). This indicates that the field-induced changes in the spectra are elastic effects rather

than permanent structural changes to gypsum. We also ruled out the possibility of spectrum evolution due to electrostatic pressure effects, as the pressure induced by E_{ext} is estimated to be ~ 0.01 GPa at $E_{\text{ext}} = 0.5$ V/nm. According to reported values²⁸, such pressure would cause shifts of only 0.01 and 0.2 cm^{-1} for O-H_A and O-H_B, respectively, which are below our detection limit.

Figure 2e summarizes the dependence of the Raman peak positions of the O-H_A and O-H_B modes on E_{ext} . The procedures for extracting peak positions are detailed in **Methods**, ‘Data analysis of Raman spectra’. O-H_A stretching mode peak position is temperature insensitive, since the E_{ext} -induced splitting remained unchanged across the measured temperatures (10 K, 80 K and 300 K). For O-H_B stretching mode, however, a red-shift from 3497 to 3481 cm^{-1} was observed at zero E_{ext} when temperature decreased from 300 K to 80 K. The FTIR peak splitting of the O-H_A stretching is summarised in **Extended Data Fig. 1**. The difference between Raman and IR peak positions at zero E_{ext} arises from the frequency mismatch of the Raman-active mode (A_g) and IR-active mode (A_u), as confirmed by our DFT calculations (see **Methods**, ‘Decoupling of the stretching frequencies of O-H bonds in crystalline water of gypsum’ and **Extended Data Fig. 3**). We also investigated the H-O-H bending mode under E_{ext} using scattering-type scanning near-field optical microscopy, as the bending mode provides direct access to the HB characteristics²⁹. However, no E_{ext} -induced peak splitting or shifting was detected, consistent with our DFT results (see **Methods**, ‘Water bending mode in gypsum’ and **Extended Data Fig. 4** for details).

Now, we recall the model at the beginning of the paper to rationalize our experimental results. First, we convert the E_{ext} -dependent stretching mode peak positions ($\omega_{\text{D-H}}$) into force constants, $k(E) = \mu\omega_{\text{D-H}}^2$, to obtain $k(E)$ as a function of E_{ext} . The total electric field acting on an O-H dipole (denoted as E_{tot}), is the sum of the internal E -field (E_{HB}) and the external electric field projected on the O-H dipole ($E_{\text{ext}} \cos \theta$):

$$E_{\text{tot}} = E_{\text{HB}} + E_{\text{ext}} \cos \theta \quad (5)$$

Here, θ is the angle between and the gypsum b-axis (**Fig. 1b**). For the dipoles O-H_A and O-H_B in gypsum, θ is 69.60° and 9.37°, respectively, as obtained from neutron diffraction data²⁶. For a free water molecule, $k(0) = 762.0 \pm 0.3$ N/m³⁰. From here, we construct a plot of $k(E)$ vs E_{tot} , **Fig. 3a**. Further details of data processing and error analysis are in **Methods**, ‘Fitting of k vs E relation in Fig. 3a and local fields at dipoles O-H_A and O-H_B’. This analysis allows us to quantify the internal electric field E_{HB} for O-H_A and O-H_B as 5.33 ± 0.63 V/nm and 3.81 ± 0.47 V/nm, respectively. From Eq. 4, we obtain the slope of $k(E)$ vs E_{tot} curve in **Fig. 3a**, the second derivative of the dipole moment along the O-H bond, $\frac{\partial^2 p}{\partial d^2} = (2.2 \pm 0.3) \times 10^{-8}$ C/m.

Similarly, we further obtain the first derivative of the dipole moment, $\frac{\partial p}{\partial d}$, using Eq. 3. To do this, we rely on existing literature data of several solid-state systems containing crystalline water, such as proton-ordered and proton-disordered ices, and solid hydrates. For free water molecule, we used the equilibrium O-H bond length obtained from fitting databases of experimental rotational energy levels^{31,32}. For neutron diffraction data we applied thermal corrections, more details are in **Methods**, ‘Thermal corrections for neutron structural data’. From here, we establish the $d(E)$ vs $E/k(E)$ relation, **Fig. 3b**, using systems for which literatures contain both neutron diffraction data to obtain O-H bond length d , and Raman spectra to get k_e and E from O-H stretching vibration frequency. Linear fitting of **Fig. 3b** gives the first derivative of dipole moment, $\frac{\partial p}{\partial d} = (7.7 \pm 1.2) \times 10^{-19}$ C (Eq. 3), and the fitted O-H bond length of a free water molecule as $d(0) = 0.9570$ Å (literature sources, details of data analysis, as well as fitting details are in **Methods**, ‘Data analysis for bond length vs E/k relation in Fig. 3b’). We then reconstruct O-H dipole moment $p(d)$ using the obtained derivatives in a Taylor expansion:

$$p(d) = \sum_{n=0}^{\infty} \frac{1}{n!} \frac{\partial^n p}{\partial d^n} (d - d(0))^n \quad (6)$$

By using the first two derivatives ($\frac{\partial^2 p}{\partial d^2}$ and $\frac{\partial p}{\partial d}$) obtained from **Figs. 3a** and **b**, and the known O-H dipole moment for a free water molecule $p(d(0)) = 1.5140 \pm 0.0004$ D³¹⁻³⁶, we plot the O-H dipole moment $p_{\text{O-H}}$ as a function of O-H bond length in **Fig. 3c**. The calculated dipole moment $p_{\text{H}_2\text{O}} = 1.88$ D for free water molecule agrees well with the reported value $p_{\text{H}_2\text{O}} = 1.8546$ D³⁴. For liquid water and ice Ih, our model predicts $p_{\text{H}_2\text{O}} = 2.66$ D and

3.35 D, respectively, which are close to the reported values of 2.9 D³⁷ and 3.09 D³⁸. For details see **Methods**, ‘Dipole moments vs O-H bond lengths in Fig. 3c’.

Further, we estimate the HB energy U_{HB} (Eq. 2) using the derived dipole moment and electric field values, given by Eqs. 6 and 4, respectively. For example, Ice Ih has a Raman shift of 3279 cm⁻¹ and a bond length of 1.014 Å (see **Methods**, ‘Data analysis for bond length vs E/k relation in Fig. 3b’). Liquid water has a bond length of 0.984 Å (see **Methods**, ‘Dipole moments vs O-H bond lengths in Fig. 3c’) and a broad O-H stretching band due to the extensive HB network, ranging from 3200 cm⁻¹ to 3650 cm⁻¹.^{39,40} Using our approach, we obtain U_{HB} per HB for ice Ih and liquid water as 10.5 (454 meV) and ~ 5 kcal/mol (~ 220 meV), respectively, consistent with reported lattice energies 7.04 kcal/mol (305 meV)^{41,42} and 5.58 kcal/mol (242 meV)⁴³.

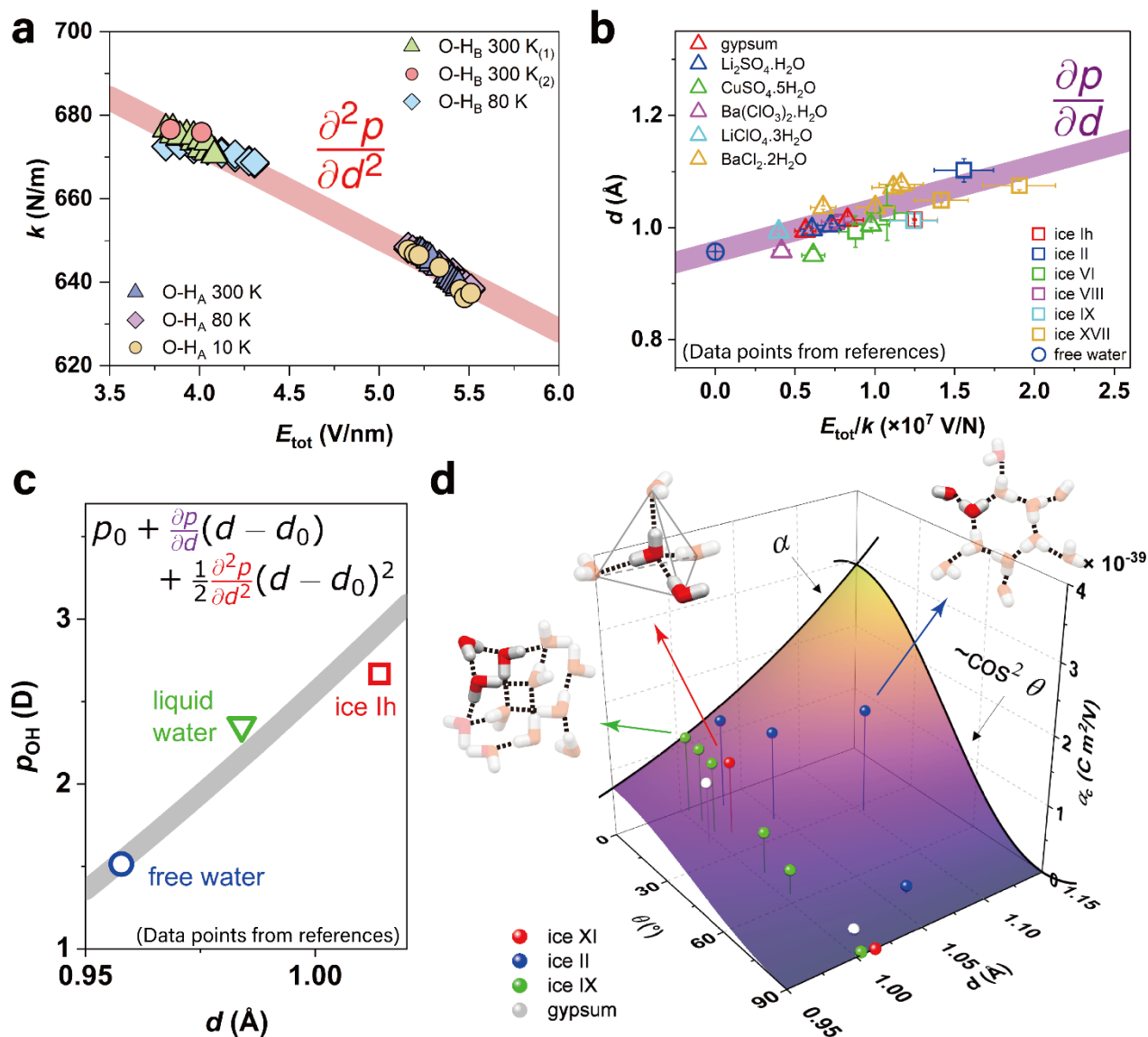


Fig. 3: Hydrogen bonding and dielectric properties of water. **a**, Force constant k vs E_{tot} along O-H bond. Symbols represent experimental results from this work using gypsum at different temperatures. The slope is the second derivative of the dipole moment along the O-H bond, $\partial^2 p / \partial d^2$. **b**, O-H bond length d versus E_{tot}/k for a range of solid-state water systems from literature (references are in **Methods**, ‘Data analysis for bond length vs E/k relation in Fig. 3b’). Linear fit gives the first derivative of the dipole moment, $\partial p / \partial d$. **c**, Estimated dipole moment along O-H bond, $p_{\text{OH}}(d)$, constructed using Eq. 6, plotted alongside with different water systems from the literature (for details and references see **Methods**, ‘Dipole moments vs O-H bond lengths in Fig. 3c’). **d**, Effective polarizability along the confining direction (α_c) of a single confined O-H dipole against the O-H bond length d and

the angle θ between the dipole and the confining direction. α is the polarizability of O-H along dipole direction ($\theta = 0^\circ$) given by Eq. 7. Red, blue, green, and grey dots represent the O-H dipoles in proton-ordered ice XI, II, IX, and gypsum. The arrows point to the structures of ice XI, II, and IX, with the geometrically non-degenerate water molecules highlighted.

Beyond HB characterisation such as dipole moment and HB energy, our approach could also predict other properties of the HB system, such as polarizability and dielectric constant. Below we show briefly the prediction power of our approach. For example, polarizability along the O-H dipole, $\alpha(d) = \partial p / \partial E$, can be evaluated using the relationship $d(E)$ from Eq. 3, as,

$$\alpha(d) = \left[\frac{\partial p}{\partial d} + \frac{\partial^2 p}{\partial d^2} (d - d(0)) \right]^3 \bigg/ \frac{\partial p}{\partial d} k(0) \quad (7)$$

Here, $\frac{\partial p}{\partial d}$ and $\frac{\partial^2 p}{\partial d^2}$ derived from our model, and $d(0)$ and $k(0)$ taken from the free water molecule (see **Methods**, ‘Fitting of k vs E relation in Fig. 3a and local fields at dipole O-H_A and O-H_B’). In nanoconfined and crystalline water systems, the rotational degrees of freedom of the dipole are restricted, meaning that no dipole reorientation under E_{ext} will contribute to the dielectric response. Therefore, Eq. 7 fully describes the polarizability of such systems. The effective polarizability along b axis is given by $\alpha_c = \alpha \cos^2 \vartheta$ and is determined by both d and ϑ , as summarized in **Fig. 3d**, along with exemplar nanoconfined water systems. For system with known bonding geometry and bond length d , the polarizability of each O-H dipole along any confining axis can be evaluated via **Fig. 3d**. And the polarizability along the confining direction can be obtained by summing up α_c for all dipoles in the system.

From here, we further extract the static dielectric constant ϵ_r of a system consisting of electrostatically confined water molecules (see also **Methods**, ‘Polarizability and dielectric behaviour of confined water’). In such a system, the polarizabilities of individual O-H dipoles add up to give ϵ_r :

$$\epsilon_r = 1 + \frac{1}{\epsilon_0} \sum_i \alpha_{ci} N_i, \quad (8)$$

where α_{ci} is the effective polarizability along confining direction and N_i is the number density of the i^{th} type of O-H dipoles. Using this relation, we obtain $\epsilon_r = 6.6 \pm 0.7$ for the confined 2D water layer in gypsum. Our capacitance measurements of gypsum crystal give $\epsilon_r = 3.68$ (see **Methods**, ‘Polarizability and dielectric behaviour of confined water’ and **Extended Data Fig. 5**). Since gypsum is an hydrogen bond heterostructure (HBH) composed of alternating CaSO₄ and water dielectrics, we can evaluate $\epsilon_r = 2.8 \pm 0.5$ for the bare CaSO₄ molecular sheets, which matches well with the reported ϵ_r of β -anhydrite, 2.7 ± 0.02 .⁴⁴

Our approach also reproduces the anomalously low $\epsilon_{r,\perp}$ of confined water, which arises from the restricted rotational degrees of freedom of liquid water under nanoconfinement⁴⁵. Here, we consider the dielectric response of confined water resulting only from electronic and atomic polarization, as described by Eq. 8. The dependence of ϵ_r along the confining direction on the orientation of water molecule is plotted in **Extended Data Fig. 6**, calculated using the density of confined water 3.39 g/cm³ from recent simulations⁴⁶. We found that when the water molecular plane is nearly parallel to the confining plane (confining angle $\theta < 23^\circ$), we can reproduce the experimentally obtained $\epsilon_{r,\perp} = 2.1$.⁴⁵

Our dipole-in- E -field approximation can be generalized to other types of electrostatic interactions beyond conventional HBs. Once the vibrational frequency of water under confinement is known, the strength of the electrostatic interaction between water and its surroundings can be evaluated. For example, interfaces between water and carbon materials often exhibit unexpected phenomena such as low friction or long slip length, which are promising for water-energy applications⁴⁷. Such electrostatic interactions between water O-H bonds and the π orbitals of sp²-hybridized carbon can be viewed as weak HBs, evidenced by red-shifts in the water stretching vibration frequency. Using our approach, we can evaluate the interaction energy between water O-H dipoles and π orbitals at graphitic surfaces.

For instance, in the case of single water molecules trapped inside a C₆₀ fullerene⁴⁸, from the measured symmetric ν_1 and antisymmetric ν_3 stretching modes at 3573 cm⁻¹ and 3659.6 cm⁻¹, we can calculate interaction strength $U_{\text{HB}} = 1.5 \pm 0.2$ kcal/mol per bond (66 ± 9 meV), comparable to typical weak HBs. Similar values are

obtained for water confined in single-walled carbon nanotubes⁴⁹. Further evidence supporting our approach comes from recent sum frequency generation (SFG) measurements at the water-graphene interface⁵⁰, where the authors reported vibration frequency of $\nu_{\text{OH}} = 3616 \text{ cm}^{-1}$ for the dangling O-H dipole. Our approach predicts the HB energy in this case is very close to that for water confined in C_{60} . More conclusively, the stretching frequency of this dangling O-H bond shows an electric field tuning effect that matches perfectly with our model (see **Methods, Extended Data Fig. 7**). More details on evaluating water-carbon interactions see **Methods, 'Water-carbon interface'**.

Our model also accurately replicates the dielectric constants for three proton-ordered ices: ice XI (ordered ice Ih), ice II, and ice IX (ordered ice III). The polarizability of O-H bonds is given by $\alpha_c = \alpha \cos^2\vartheta$ and Eq. 7, as shown in **Fig. 3d** (see also **Methods, 'Dielectric constants of water ice systems'**). For bulk liquid water, using the dipole moment from Eq. 6 and considering rotational averaging, we obtain $\epsilon_r = 27 \pm 2$, which is much lower than experimental value of 79 (see **Methods, 'Dielectric constant of liquid water'**). This discrepancy arises because the rotations of water molecules are not independent of each other, an effect usually accounted for by introducing the dipole correlation factor G_k .⁵¹ To reproduce the experimentally obtained ϵ_r , $G_k \approx 3.15$ is needed in our case, which is close to the calculated value of 2.2 ± 0.2 for bulk liquid water^{52,53}. Our model also cannot predict the anomalously high dielectric constant in proton-disordered ices, such as ϵ_r on the order of 100 for ice Ih, the most common form of ice in nature^{54,55}. This behaviour is usually attributed to the presence of defects in the form of partial rotations and proton jumps, which form polarized domains at lower temperatures where ice sometimes becomes ferroelectric⁵⁶.

In summary, our dipole-in- E -field approach reliably quantifies the characteristics of confined water molecules in various complex environments, advancing our understanding of HB in biologically and technologically relevant systems. Using coefficients parametrized from this work, we can quantitatively evaluate properties such as O-H bond length, local electric field, dipole moment, HB strength, polarizability, and dielectric constant directly from spectroscopic data (Raman, FTIR, or SFG) for a wide range of water systems, including crystallohydrates, ices, and nanoconfined water. This approach can be extended beyond confined water to systems such as organic molecules, (bio)polymers, liquid phases, and electrochemical interfaces, which are crucial for bio-medicine and technology. Testing the limits of our approach in scenarios where quantum and many-body effects dominate, such as blue-shifting strong HBs⁶ or cooperative HB systems⁵⁷, could provide new insights into the fundamental nature of hydrogen bonding.

Notably, our work represents the first study of hydrogen bond heterostructures (HBHs), which could emerge as a new class of intelligent materials allowing for facile assembly and fabrication, similar to van der Waals materials. HBHs offer unique properties, including electrical and chemical tunability, stronger and more directional bonding compared to van der Waals forces, and the potential for self-assembly and emergent phenomena. By complementing hydrogen-bonded organic frameworks, HBHs and HB technology could enhance applications in gas separation, catalysis, and (opto)electronic devices¹³⁻¹⁸. The combination of our dipole-in- E -field approach and the development of HBHs opens new avenues for the rational design and precise control of the properties of hydrogen-bonded systems.

Methods

Full form of the dipole-in- E -field approximation

The 3D form of Hooke's law can be written as $\mathbf{F} = -\boldsymbol{\kappa} \cdot \mathbf{X}$. Here \mathbf{X} is the displacement vector in 3D space, and $\boldsymbol{\kappa}$ is a 3×3 strain stiffness tensor, where the diagonal and off-diagonal indices are the stiffness in directions parallel and normal to each force components. The potential energy of a harmonic oscillator in 3D case is:

$$U_{osc} = \frac{1}{2} \mathbf{X}^T \cdot \boldsymbol{\kappa} \cdot \mathbf{X} + U_E, \quad (9)$$

$$U_{HB} = -\mathbf{p} \cdot \mathbf{E} + \dots \quad (10)$$

Set x-axis along D-H bond, then we have electrostatic force and sum potential stiffness: $\mathbf{F}(\mathbf{E}) = -\nabla U_{\text{HB}}$ and $k(\mathbf{E}) = \nabla^2 U_{\text{osc}}$. The field-dependent bond length and field-dependent spring constant are then:

$$\mathbf{d}(\mathbf{E}) = \mathbf{d}(0) + \nabla \mathbf{p} \cdot \mathbf{E} \frac{1}{k(\mathbf{E})} \quad (11)$$

$$k(\mathbf{E}) = k(0) - \nabla^2 \mathbf{p} \cdot \mathbf{E} \quad (12)$$

In this work, we consider only the parallel response along D-H bond. Thus, among the nine indices of κ , only one diagonal term is non-zero. The system then simplifies to the 1D problem described in the main text.

Device fabrication

Gypsum films were isolated from bulk natural crystals onto SiO₂ (290 nm)/Si and CaF₂ substrates (for spectroscopic measurements) and polydimethylsiloxane (PDMS) stamps (for heterostructure fabrication) using micromechanical exfoliation in cleanroom. Graphite/gypsum/graphite heterostructure is fabricated using all-dry viscoelastic stamping technique⁵⁸: first, graphite flake (bottom electrode) was isolated from natural graphite crystal onto SiO₂/Si substrate; gypsum flake and top graphite electrode were exfoliated onto PDMS stamp. The gypsum and top graphite flakes were then transferred onto bottom graphite electrode successively, aligning and stacking target flakes under the optical microscope using transfer rig.

Gypsum is prone to dehydration in vacuum or when exposed to elevated temperature, therefore, conventional lithography and metal deposition process cannot be used to fabricate electrical contacts to gypsum. Instead, we used two thick graphite flakes with over 100 μm length as extended electrical contacts to the top and bottom FLGs of the heterostructure, to which gold wires were then attached using conductive silver paint. For devices with hBN separation layers, the hBN flakes were exfoliated and transferred using the techniques described elsewhere⁵⁹.

Vibrational spectroscopy measurements

Angular-resolved polarized Raman spectroscopy was performed using Oxford WITec alpha300R confocal Raman system, with 600 lines/mm grating and a 532 nm wavelength laser with linear polarization. During measurements, the sample was fixed on the sample stage, with incident laser polarization rotated by a polarizer at a step of 5°. The spectra were taken with parallel analyser configuration at each incident orientation, so the collected light had the same polarization direction as incident. For each spectrum, the acquisition time was 10 seconds with 6 accumulations.

Raman measurements under electric field in ambient conditions were carried out using Renishaw inVia confocal Raman system equipped with 2400 lines/mm grating and 514 nm linearly polarized laser, focused through a $\times 100/0.90$ NA objective. The voltage was applied using a Keithley 2614B source meter.

Peak splitting is not very pronounced even at 0.3 V/nm (e.g., **Extended Data Fig. 8** for O-H_A stretching mode), but higher field is unreachable at ambient conditions due to field-induced degradation of FLG electrodes, even with hBN spacers. So, we performed Raman measurement at $T < 80$ K, where E_{ext} of up to 0.5 V/nm can be applied and distinct peak splitting is well resolved. Raman measurements at cryogenic temperatures were performed on WITec alpha300 R Raman system with 600 lines/mm grating and $\times 100/0.85$ NA objective. The sample was placed in an Oxford microstat system in vacuum with temperature controlled by a liquid N₂ circulation loop for measurements at 80 K and liquid He for measurements at 10 K. The fluctuation of temperature was ± 5 K.

Fourier transform infrared (FTIR) spectra were recorded with a Bruker VERTEX 80 spectrometer equipped with a Bruker HYPERION 3000 FTIR microscope. For low temperature FTIR measurements at 83 K, the sample was placed in a Linkam stage with temperature controlled by a liquid N₂ circulation loop. All spectra were collected with 4 cm^{-1} resolution and averaged over 512 scans.

Nano-FTIR measurements were performed on an AFM based scattering-type scanning near-field optical microscopy (s-SNOM) from neaspec GmbH. The conventional Pt/Ir probe (ARROW-NCPT-50, Nanoworld) with a tapping frequency of 270 kHz was illuminated with a p-polarized mid-infrared broadband difference frequency generation (DFG) laser (frequency range 1000 – 1900 cm^{-1} , average power < 1 mW). The sample for s-SNOM measurements was FLG/gypsum/FLG stack on SiO₂/Si substrate. During measurements, a dc voltage was

applied to bottom graphite electrode, while the top graphite and AFM probe were electrically grounded, creating an electric field along out-of-plane direction. Obtained nano-FTIR spectra were collected at different voltage levels by averaging 30 interferograms (spectral resolution $\approx 7 \text{ cm}^{-1}$) with 2048 pixels and an integration time of 10 ms/pixel. All spectra are normalized to that of a Si substrate.

Data analysis of Raman spectra

For **Fig. 1f** in the main text, we first performed background subtraction on raw spectra using 2nd polynomial with 256 sample points, followed by peak fitting using Voigt function. The peak position and peak width of water stretching modes were constrained within $3400 - 3412 \text{ cm}^{-1}$ and $20 - 50 \text{ cm}^{-1}$ for O-H_A, and $3490 - 3500 \text{ cm}^{-1}$ and $20 \text{ cm}^{-1} - 70 \text{ cm}^{-1}$ for O-H_B. Raman spectra in **Fig. 2** (main text) were obtained first through baseline fitting and subtraction using 4th polynomial with 256 sample points, followed by peak fitting using Voigt function. Initial peak positions were set at the position with maximum intensity. The peak widths were limited within 100 cm^{-1} and 90 cm^{-1} respectively.

Decoupling of the stretching frequencies of O-H bonds in crystalline water of gypsum

In gypsum, water O-H covalent bonds are stretched due to HB. Different crystalline environment of the two O-H bonds results in a distorted asymmetric water molecule. Such asymmetry decouples and localizes the normal symmetric and antisymmetric stretching onto individual O-H bonds. Consequently, one O-H bond will have much larger vibration amplitude than the other in each vibration mode.

We performed density functional theory (DFT) calculations using Quantum ESPRESSO package, to elaborate on the vibrational response of gypsum. Dispersion corrections that account for the van der Waals forces were incorporated following the empirical D3 formulation by Grimme, yield 0.06% difference with experimental lattice parameters. Calculations of phonon frequencies were carried out using the finite difference methodology implemented in Phonopy by displacing each atom 0.001 \AA along three principal axes. Generalized Gradient Approximation (GGA) formulation by Perdew, Burke and Ernzerhof was used to model exchange-correlation interactions among electrons in all the calculations. An energy cutoff of 65 Ry with a uniform Monkhorst-pack k-mesh of $5 \times 5 \times 5$ is used for all the calculations on the primitive unit cell. Convergence criteria used for all self-consistent field calculations are 10^{-10} Ry per formula unit.

In gypsum crystal, water has 8 stretching modes in total, **Extended Data Fig. 3**. According to our DFT calculations, they are grouped into two branches, high- and low-frequency (near 3500 cm^{-1} and 3400 cm^{-1}), with vibration amplitudes mainly localized on O-H_B and O-H_A bonds, respectively. In each of these two branches, the four levels arise due to the symmetry of gypsum crystal. In particular, four water molecules in a unit cell are grouped into two inversion symmetric pairs. Each of the two water molecules in the pair vibrate collectively either in-phase or out-of-phase, which decouples the modes. In turn, each in-phase and out-of-phase modes has symmetric and anti-symmetric intramolecular solutions, which leads to further mode decoupling.

Infrared spectroscopy of water O-H_A stretching modes in gypsum

Similar to Raman data presented in **Fig. 2** in main text, peak broadening and splitting were also observed in low temperature FTIR measurements (**Extended Data Fig. 1**). The IR peak of O-H_A mode blue-shifted from 3401 cm^{-1} to 3412 cm^{-1} when temperature reduced from 300 to 80 K, possibly due to a volumetric contraction effect which shortens the effective O-H bond length.⁶⁰ Similarly to Raman, the O-H_A stretching splits into two peaks, corresponds to the two O-H_A A modes in **Extended Data Fig. 1b** (A_g^A and A_u^A at zero field, **Extended Data Fig. 3**). The obtained electric field dependence of stretching peak position in FTIR spectra is similar to that of our Raman results.

Due to the large overlap between the two E_{ext} induced O-H_A peaks, we instead chose positions of maximal peak intensity for spectra fitting. At high E -fields, both O-H_A peaks show similar splitting with electric field. However, at low E fields, the low-frequency peak is nearly E -field independent. According to our DFT calculations, the two

O-H_A peaks correspond to two A modes of O-H_A at 3406 and 3393 cm⁻¹, which are only Raman-active (A_g^A mode) and IR-active (A_u^A mode) at zero field, respectively. They are not the same mode and have different frequency. This accounts for the absence of A_g^A mode in IR and A_u^A mode in Raman at zero field, and the deviation of IR data from linear splitting at low E_{ext}-field (< 0.065 V/nm) in **Extended Data Fig. 1c**.

Water bending mode in gypsum

Due to extremely low Raman intensity, water bending mode and its field-dependence were investigated via nano-FTIR measurements using scattering-type scanning near-field optical microscopy (sSNOM). Water in gypsum exhibits two bending modes located around 1620 cm⁻¹ and 1680 cm⁻¹, **Extended Data Fig. 4**. This agrees well with our DFT calculations. The water bending mode also decouples into four sub-modes, because of four water molecules in a gypsum unit cell. Similar to the stretching vibration mode decoupling, inversion symmetry divides these four modes into two pairs, with frequencies around 1620 cm⁻¹ and 1680 cm⁻¹. We did not observe any *E*-field response for the bending modes, **Extended Data Fig. 4**. This is consistent with our DFT calculations, which show that bending mode frequencies do not change even at a high electric field up to 1.8 V/nm, because phonon dispersion around Γ point was unaffected by external electric field.

Fitting of *k* vs *E* relation in Fig. 3a and local fields at dipole O-H_A and O-H_B

The *k* vs *E* relation in **Fig. 3a** in the main text was obtained by accounting for the applied E_{ext} component with respect to O-H dipoles and accommodating the crystal structure symmetry of gypsum, using data from **Fig. 2e**, main text. To this end, the E_{ext} for each dataset was scaled by cos θ to obtain the electric field component along each O-H dipole. Here θ (as defined in **Fig. 1b**, main text) is 69.60° and 9.37° for O-H_A and O-H_B dipoles, respectively²⁶. Then, half of each dataset (those with positive slopes) were flipped horizontally, so that all the datasets having negative slope (red-shift). According to Eq. 4 in main text, this slope corresponds to $-\frac{\partial^2 p}{\partial d^2}$, where *E* is the total electric field at the dipole, equal to E_{HB} + E_{ext}. All datasets transformed by the above procedure were then fitted globally using Eq. 13 with three fitting parameters – one is the shared slope $\frac{\partial^2 p}{\partial d^2}$ for both O-H_A and O-H_B data because $\frac{\partial^2 p}{\partial d^2}$ is expected to be the same for both dipoles, and two different E_{HB} for O-H_A and O-H_B due to the different local HB field:

$$k(E) = k(0) - \frac{\partial^2 p}{\partial d^2} (E_{\text{HB}}^{\text{A(B)}} + E_{\text{ext}} \cos \theta) \quad (13)$$

To obtain the intercept *k*(0) in Eq. 4 in main text (and Eq. 13), we resorted to the known data on water in gas phase from literature. Vibrational spectroscopy of free water molecules is complicated: three vibrational modes – symmetric ν_1 and antisymmetric ν_3 stretching and bending mode ν_2 together with numerous rotational modes result in hundreds of thousands of peaks of various intensities and linewidths⁶¹⁻⁶⁴. The most recent values of free H₂¹⁶O molecule's vibrational transition frequencies from the W2020 database are 3657.053, 3755.929, and 1594.746 cm⁻¹, for ν_1 , ν_3 , and ν_2 , respectively³⁰. The vibration energy of uncoupled O–H bond $\nu_{\text{O-H}}$, estimated as the average of ν_1 and ν_3 , is 3706.491 cm⁻¹, in good agreement with $\nu_{\text{O-H}} = 3707.467$ cm⁻¹ for HD¹⁶O molecule, where decoupling is provided by a large mismatch in effective masses of H and D⁶⁵. This gives us the harmonic spring constant $k(0) \approx 762.0 \pm 0.3$ N/m for uncoupled O–H bond in HB-free water. Linear fitting using Eq. 13 gives slope $-\frac{\partial^2 p}{\partial d^2} = (2.23 \pm 0.26) \times 10^{-8}$ C/m. The local E_{HB}-fields at O-H_A and O-H_B dipoles are (5.33 ± 0.63) and (3.81 ± 0.47) V/nm, respectively. The uncertainty is given by the 2 σ value of the linear fit (reduced $\chi^2 = 2.3$).

Thermal corrections for neutron structural data

Bond lengths from neutron diffraction are based on time-averaged neutron scattering intensity, giving an averaged interatomic separation. The actual bond length is slightly longer, after applying thermal corrections. The thermally corrected O-H bond lengths in **Fig. 3b** in the main text were obtained in different ways. For ice Ih, ice VIII, ice IX, Li₂SO₄·H₂O, Ba(ClO₃)₂·H₂O, and LiClO₄·3H₂O, their thermally corrected O-H bond lengths were

provided in the respective references. For ice II, ice VI, ice VIII and ice XVII, the thermal corrections were evaluated using isotropic temperature factor, B . For $\text{CuSO}_4 \cdot 5\text{H}_2\text{O}$ and $\text{BaCl}_2 \cdot 2\text{H}_2\text{O}$, thermal corrections were carried out using anisotropic temperature factors, β_{ij} . The temperature parameters of the systems are given in corresponding references respectively. The approaches used to evaluate the thermal corrections were reported in Ref. ⁶⁶.

Data analysis for bond length vs E/k relation in Fig. 3b

The various systems in **Fig. 3b**, main text contain ices and solid hydrates. The distance between H and metal ions (M) in most solid hydrates ranges from 1.5 - 3 Å. Here, we focused on pure hydrogen bonding interactions and analysed the solid hydrates systems with H...M distance of 2 - 3 Å, ignoring materials such as $\text{BeSO}_4 \cdot 4\text{H}_2\text{O}$, where the significantly shorter H...Be distance of 1.6 Å may affect the charge distribution on H via electrostatic interactions from Be cation. All O-H bond lengths are from thermally corrected neutron diffraction data. Where the O-H length was measured on deuterated water D_2O , the thermal-corrected bond length is further upshifted by 3% to account for the bond difference between H_2O and D_2O ⁶⁷. For vibrational spectroscopy data on systems with multiple stretching peaks, we assigned peaks to O-H bonds with different bond lengths such that a shorter bond has a higher vibration frequency due to the steeper potential profile. The assignment process for each confined-water system is discussed below and data is summarized in **Extended Data Table 1**.

For ice Ih, one Raman peak is observed at 3279 cm^{-1} for 3 mol% HOD ice at 123 K, corresponds to the stretching vibration of O-H bond, free of intra-molecule coupling due to large differences in the atomic mass of H and D ⁶⁸. Two O-H bond lengths of $(1.008 \pm 0.002) \text{ Å}$ and $(1.004 \pm 0.001) \text{ Å}$ given by neutron diffraction at 123 K were thermally corrected by $+0.008 \text{ Å}$ and averaged to $(1.014 \pm 0.0011) \text{ Å}$ ⁶⁹.

For ice II, two strong Raman peaks were found at 3194 cm^{-1} and 3314 cm^{-1} at 77 K ^{70,71}. Neutron diffraction of D_2O ice II gives four O-D bond lengths of $(1.014 \pm 0.020) \text{ Å}$, $(0.975 \pm 0.020) \text{ Å}$, $(0.956 \pm 0.020) \text{ Å}$ and $(0.937 \pm 0.020) \text{ Å}$ on two symmetrically non-degenerated water molecules at 110 K, with isotropic temperature parameter (B) of 4.5 Å^{-2} for both O and D ⁷². The O-D bond lengths were thermal-corrected using B , and upshifted further by 3% for the D-H conversion. The final O-H bond lengths in ice II are $(1.102 \pm 0.021) \text{ Å}$, $(1.064 \pm 0.021) \text{ Å}$, $(1.046 \pm 0.020) \text{ Å}$ and $(1.028 \pm 0.021) \text{ Å}$. The low frequency peak at 3194 cm^{-1} is assigned to the local stretching of the longest O-H bond of 1.102 Å . The stretching vibration can be coupled both intra- and intermolecularly among the remaining three O-H bonds due to their close bond lengths, resulting in uncertainty in vibration frequency assignment. Hence, we excluded these three data points and only focused on the longest bond.

Ice VI contains two types of O_4 octahedra structure interpenetrating into each other, revealed by the neutron diffraction of D_2O ice. ⁷³ For the first O_4 octahedra network, all proton positions are equivalent, yielding one O-D bond length $(0.986 \pm 0.048) \text{ Å}$, indicating a strong intramolecular coupling in stretching vibration. The second O_4 octahedra structure has three O-D bond lengths at $(0.937 \pm 0.055) \text{ Å}$, $(0.976 \pm 0.051) \text{ Å}$ and $(0.939 \pm 0.032) \text{ Å}$ with multiplicity 1, 1 and 2, yielding an average of $(0.951 \pm 0.027) \text{ Å}$. These two bonds are thermal-corrected to $(0.996 \pm 0.048) \text{ Å}$ and $(0.961 \pm 0.027) \text{ Å}$ using $B = 2.99 \text{ Å}^{-2}$ for oxygen and 3.80 for hydrogen ⁷³, and further upshifted to $(1.026 \pm 0.049) \text{ Å}$ and $(0.993 \pm 0.028) \text{ Å}$ for the D-H conversion. These two bonds are associated with Raman stretching modes at 3390 cm^{-1} and 3329 cm^{-1} . ⁷⁴

For ice VIII, only one bond length is given at $(0.969 \pm 0.007) \text{ Å}$ in D_2O ice at 10 K ⁷⁵, which is thermal-corrected to $(0.981 \pm 0.007) \text{ Å}$ using $B = 0.58 \text{ Å}^{-2}$ for O and 1.54 for D, and further upshifted to $(1.010 \pm 0.009) \text{ Å}$ because of D-H conversion. The O-H Raman vibration frequency is taken as the average of three intramolecular-coupled normal modes locating at 3477.4 cm^{-1} ($\nu_1\text{B}_{1g}$), 3447.6 cm^{-1} ($\nu_3\text{E}_g$) and 3358.8 cm^{-1} ($\nu_1\text{A}_{1g}$) at 100 K ⁷⁶, which is 3427.9 cm^{-1} .

Ice IX is a proton-ordered phase. Neutron diffraction data on D_2O ice shows that protons are preferably arranged in one configuration (referred to as 'major site'), with a nonzero occupancy on the other configuration (referred to as 'minor site'). The O-D lengths for major and minor configurations are $(0.976 \pm$

0.003) Å and (1.02 ± 0.06) Å. Thermal-corrected length is reported for only the major site at (0.983 ± 0.004) Å.⁷⁷ This value is further upshifted to (1.012 ± 0.004) Å for D-H conversion. Because of the low occupancy, we exclude the minor configuration bond length and only use that of the major configuration. Two intense Raman peaks of O-H stretching are found at 3280.7 cm⁻¹ and 3160.4 cm⁻¹ at 100 K⁷⁸, with the latter assigned to the vibration of O-H bond on major sites.

For ice XVII, two O-H stretching Raman peaks at 3106.3 cm⁻¹ and 3231.8 cm⁻¹ are reported in ref.⁷⁹. These are regarded as decoupled vibration because their separation is > 100 cm⁻¹. Two O-D bond lengths are given by neutron diffraction on D₂O ice at (1.023 ± 0.007) Å and (1.006 ± 0.004) Å, which are thermal-corrected to (1.044 ± 0.007) Å and (1.018 ± 0.004) Å using $B = 2.37 \text{ Å}^2$ for O, 4.05 Å² for D1 and 3.34 Å² for D2, respectively⁸⁰. These values are further upshifted to (1.075 ± 0.007) Å and (1.049 ± 0.004) Å for D-H conversion.

For CaSO₄·2H₂O (gypsum), the Raman frequency of O-H stretching is taken from this work, which is 3406 cm⁻¹ and 3484 cm⁻¹, measured at room temperature. The O-H bond lengths are taken from ref.²⁶, (0.961 ± 0.006) Å and (0.948 ± 0.004) Å at 320 K, which are thermal-corrected to (0.984 ± 0.006) Å and (0.966 ± 0.004) Å using $B = 1.749 \text{ Å}^2$ for O, 3.520 Å² for D1 and 3.074 Å² for D2, respectively. These values are further upshifted to (1.014 ± 0.006) Å and (0.995 ± 0.004) Å for D-H conversion.

For Li₂SO₄·H₂O, two thermal-corrected O-H bond lengths are (1.004 ± 0.003) Å and (0.997 ± 0.002) Å.⁸¹ We associate these two bonds with two Raman peaks of O-H stretching at 3439 cm⁻¹ and 3480 cm⁻¹, respectively.⁸²

CuSO₄·5H₂O contains five water molecules per unit cell, among which four are coordinated to Cu²⁺, and the remaining one is far away from Cu²⁺ thus non-coordinated. To exclude the interactions with metal ions, we only focus on the non-coordinated water molecules in this study. CuSO₄·5H₂O exhibits multiple water stretching peaks, and the modes above 3300 cm⁻¹ is assigned to the stretching of non-coordinated water molecules, at 3360 cm⁻¹ and 3477 cm⁻¹.^{83,84} The O-H bond lengths of the non-coordinated water molecules are (0.978 ± 0.005) Å and (0.936 ± 0.011) Å.⁸⁵ These values are corrected for thermal motion using anisotropic temperature parameters tensor (β_{ij}) to (1.005 ± 0.005) Å and (0.951 ± 0.011) Å. These two bonds are associated with 3360 cm⁻¹ and 3477 cm⁻¹ Raman peaks, respectively.

For Ba(ClO₃)₂·H₂O, a single thermal-corrected O-H bond length is reported at (0.958 ± 0.011) Å⁸⁶, suggesting an intramolecularly coupled vibration. Thus the vibration frequency is taken as the average between ν_1 (3512 cm⁻¹) and ν_3 (3582 cm⁻¹) vibration modes at 90 K⁸⁷, that is 3547 cm⁻¹.

For LiClO₄·3H₂O, the O-H bond length is taken as the average among three refinement series, (0.993 ± 0.004) Å, with uncertainty coming from the standard deviation of the three series.⁸⁸ The values provided in the reference have been thermal corrected during refinement. This bond length is associated with a sharp Raman peak in water stretching region, 3553 cm⁻¹.⁸⁹

For BaCl₂·2H₂O, four O-H bond lengths are given by neutron diffraction measurements at (0.953 ± 0.003) Å, (0.959 ± 0.003) Å, (0.960 ± 0.003) Å, and (0.972 ± 0.004) Å.⁹⁰ These values are thermal corrected to (1.0359 ± 0.003) Å, (1.0364 ± 0.003) Å, (1.0717 ± 0.003) Å and (1.077 ± 0.004) Å using β_{ij} . and assigned to four intermolecularly uncoupled Raman modes at 3456 cm⁻¹, 3352 cm⁻¹, 3318 cm⁻¹ and 3303 cm⁻¹.⁹¹

The assignment and references are given in Extended Data Table 1, with all the data points plotted in **Fig. 3b** in the main text. The data points above were then fitted using a linear function with both X and Y errors, yielding a slope of $(7.83 \pm 1.26) \times 10^{-19} \text{ C}$ and intercept of (0.957 ± 0.001) Å, corresponding to $\frac{\partial p}{\partial d}$ and $d(0)$ in Eq. 3 in the main text. The uncertainty corresponds to 2 σ . The reduced χ^2 for this fitting is 4.96.

Dipole moments vs O-H bond lengths in Fig. 3c

In the gas phase, equilibrium dipole moment of H₂O molecule is 1.855 ± 0.001 D, given by Stark effect measurements³⁴. The H–O–H angle in gas phase is 104.48° and the O–H bond length is 0.9578 Å, as determined

by fitting experimental rotational energy levels with the rotation-vibration Hamiltonian³¹. This gives a dipole moment of the O–H bond $p_{\text{OH}} = 1.514 \pm 0.001$ D.

Effective dipole moment of liquid water at ambient conditions is 2.9 ± 0.6 D, estimated from $0.5e$ ($\pm 20\%$) charge transfer along each O–H bond, using synchrotron x-ray diffraction measurements³⁷. The H–O–H angle and the O–H bond length are 103.924° and 0.984 Å, obtained from a joint refinement of X-ray and neutron diffraction data⁹². No iso- or anisotropic temperature parameters available, so no correction was made to the O-H bond length. This gives dipole moment of O-H bond $p_{\text{OH}} = 2.4 \pm 0.5$ D.

Ice Ih has a dipole moment of 3.09 ± 0.04 D, calculated using multipole iterative method, with error extracted from Fig. 1 in the reference.³⁸ The O-H bond length and H-O-H angle are 1.014 Å and 109.21° from neutron diffraction data at 60 K. The bond length is further thermal corrected to 1.0125 Å.⁶⁹ The p_{OH} is calculated to be 2.67 ± 0.04 D.

Polarizability and dielectric behaviour of confined water

We consider a dielectric with $\epsilon_r = \epsilon/\epsilon_0$ consisting of polarizable dipoles with the polarizability along the field direction $\alpha_{c,i}$ and the number density of dipoles N_i . The polarization under the electric field E is $P = (\epsilon_r - 1)\epsilon_0 E$, which equals to the sum of the polarization from all dipoles, $P = \sum_i \alpha_{c,i} E N_i$, here i denotes different types of dipoles. This leads to Eq. 8 in the main text, the dielectric constant of a confined water system. From Eqs. 1, 2 and 6 in the main text, polarizability can be written in terms of total electric field E along O-H bond:

$$\alpha(E) = \frac{\left(\frac{\partial p}{\partial d}\right)^2 k_0^2}{\left(k_0 - \frac{\partial^2 p}{\partial d^2} E\right)^3} \quad (14)$$

Taking gypsum as an example of nano-confined water system, the polarizability of the four types of O-H dipoles in gypsum are doubly degenerated and dictated by the local E_{HB} field, 5.33 and 3.81 V/nm for O-H_A and O-H_B, respectively. In the presence of external electric field, the four dipoles have four different local fields, and thus the structure symmetry is broken, resulting in two polarizabilities splitting towards two directions (**Extended Data Fig. 5c**). By adding up the four field-dependent polarizabilities according to Eqs. 7 and 8 in the main text, dielectric constant $\epsilon_r = 6.6 \pm 0.7$ was obtained for water in gypsum. The calculated field-tunable $\epsilon_r(E)$ is plotted in **Extended Data Fig. 5d**, which presents a modulation of $< 0.1\%$ due to the field-tuning effect on confined water layers in gypsum.

To observe the field-tunable $\epsilon_r(E)$ in gypsum, we performed capacitance measurements in one of our devices, using capacitance bridge (**Extended Data Fig. 5a**). In the measurement, a graphite/gypsum/graphite capacitor fabricated on SiO₂ (290 nm)/Si substrate was placed in vacuum ($< 10^{-6}$ mbar). The capacitance of the device was measured using AH 2700 capacitance bridge with an ac excitation of 1 V at 1.2 kHz.

The equivalent circuit is sketched in **Extended Data Fig. 5a**. The experimental capacitance measured by the bridge is a combination of four capacitors with three contributions: capacitance of the gypsum (C_g), quantum capacitance of top and bottom graphite electrodes (C_q), and parasitic capacitance from the measurement setup (C_p). From capacitors model we can fit the experimental curve using:

$$C = C_p + \frac{1}{1/C_{q1} + 1/C_{q2} + 1/C_g} \quad (15)$$

Field-independent C_p is a fitting parameter with constant value. ϵ_r , which is embedded in C_g , another fitting parameter. $1/C_{q1}$ and $1/C_{q2}$ are function of carrier density on graphite electrodes and are given by Ref. ⁹³, and we obtain $C_p \approx 319$ fF and $\epsilon_r \approx 3.68$. With C_p subtracted from the experimental curve, the modulation of capacitance is $\sim 0.9\%$, much higher than the 0.1% modulation expected for field-tunable polarizability of confined water. Thus, it is concluded that the effect of field-tunable polarizability of water molecules is hidden in the graphite quantum capacitance.

Gypsum is a HBH consisting of confined water layers and CaSO₄ layers, which can be modelled as two capacitors in series. The total ϵ_r of gypsum has been determined above. The capacitance of confined water layers can be evaluated using number density of confined water molecules and Eq. 8 in the main text. Gypsum

(CaSO₄·2H₂O) has molecular weight of 172.17 g·mol⁻¹ and mass density 2.32 g·cm⁻³⁹⁴, yielding a number density of 8.11 × 10²⁷ m⁻³ of gypsum, and 1.62 × 10²⁸ m⁻³ of H₂O. Considering that the water molecules are confined between CaSO₄ layers, with confining space taking up 40% of the gypsum volume (confining length measured between O_s and O_s', the oxygen atoms in SO₄ groups from adjacent layers). The number density of water molecules in the confining space is corrected to 4.06 × 10²⁸. Eq. 8 in the main text produces ε_r = 6.6 ± 0.7 for confined 2D water layers in gypsum. Using capacitor-in-series model, ε_r = 2.8 ± 0.5 can be obtained for CaSO₄ molecular sheets. This value matches well the reported ε_r for anhydrite (CaSO₄), which is 2.45 ± 0.52 for γ-phase and 2.70 ± 0.02 for β-phase.⁴⁴

Our model finds that water sheets confined in gypsum presents a lower ε_r compared to its bulk form due to the restricted rotational freedom. Such behaviour is similar to water confined in carbon nanotubes (CNT). Simulations has shown that in CNT-confined water, axial component of ε_r increases to above 100 with a relaxation time longer than bulk water, while the ε_r of water normal to the carbon walls decreases drastically (to ~6), with the dipolar relaxation time severely suppressed.^{95,96} The small normal component of ε_r is attributed to the restricted dipole rotation, caused by the strong orientation of water molecules near walls due to induced surface charge.⁹⁷ A similar decrease in ε_r was also found at the water—C₆₀ fullerenes interface, which is attributed to the electrostatic interaction between water and surface charge on C₆₀.^{98,99}

Dielectric constant of liquid water

We consider the dielectric response of liquid water coming from two parts: dipole reorientation, as well as atomic and electronic polarization. The former is given by Langevin-Debye equation¹⁰⁰:

$$\langle P_{dipole} \rangle = \frac{N_0 p^2 E}{3kT} \quad (16)$$

where N_0 and p are the number density and dipole moment of the H₂O molecule, k is Boltzmann constant, T the temperature and E is the electric field. The number density of H₂O molecule is 3.35 × 10²⁸ m⁻³, using the mass density of liquid water. The latter, atomic and electronic polarization, is given by considering individual O-H dipole moments of number density $2N_0$ and dipole moment p , with orientation given by Boltzmann distribution of p in external E-field. The induced dipole moment per O-H bond is $\alpha E (\cos \vartheta)^2$, where θ is the angle between p and E (defined in **Fig. 1b**, main text). Integration over all 3D space gives the polarization density of induced dipole:

$$P_{a+e} = 2\alpha E N_0 \frac{\int_1^{-1} y^2 e^{xy} dy}{\int_1^{-1} e^{xy} dy} \quad (17)$$

With $y = \cos \theta$, and $x = pE/kT$. Using Taylor expansion on the integral term and keeping to quadratic term, Eq. 17 reduces to

$$P_{a+e} = 2\alpha E N_0 \left[\frac{1}{3} + \frac{1}{45} \left(\frac{pE}{kT} \right)^2 \right] \quad (18)$$

Adding up the two contributions and using $P = (\epsilon_r - 1)\epsilon_0 E$, we obtain dielectric constant of liquid water:

$$\epsilon_r = 1 + \frac{N_0}{3\epsilon_0} \left[\frac{p^2}{kT} + 2\alpha + \frac{2\alpha}{15} \left(\frac{pE}{kT} \right)^2 \right] \quad (19)$$

Where p and α are be given by our model from Eqs. 6 and 7 in the main text.

Our model successfully reproduced the dipole moment of liquid water 2.66 D. using this results and Eq. 7 in the main text, a static dielectric constant ε_r = 27 ± 2 was obtained for liquid water. This is significantly lower than experimental value ε_r = 79 due to the complex hydrogen bonding network of water clusters in liquid water, which enhances the interaction between water molecules and thus affects the dielectric response. A conventional approach to include such correlation effect is to multiply p^2/kT term in Eq. 19 with a dipole correlation factor G_k .⁵¹ To get experimental ε_r = 79, G_k of 3.15 should be taken, close to the reported $G_k = 2.55$.^{52,53} With bond length taken as 0.984 Å⁹², our model yields a dielectric constant value of 78.7 ± 7.2 at $E = 0$ V/nm and 78.8 ± 7.2 at $E = 0.5$ V/nm, with the electronic polarization contributes to only 3% of the dipole reorientation.

Water-carbon interface

In the case of single water molecules trapped inside a C₆₀ fullerene, both the symmetric ν_1 and antisymmetric ν_3 stretching modes are significantly red-shifted compared to free H₂O, to 3573 cm⁻¹ and 3659.6 cm⁻¹, respectively. In a harmonic approximation, this corresponds to a force constant $k \approx 725$ N/m. Using Eqs. 3 and 4 in the main text, we obtain a local E -field $E_{\text{HB}} = 1.7 \pm 0.2$ V/nm, O-H bond length $d_{\text{OH}} = 0.974 \pm 0.004$ Å, and dipole moment (using Eq. 6 in the main text) $p_{\text{H}_2\text{O}} = 2.37 \pm 0.14$ D. With our dipole-in- E -field model, the calculated interaction strength $U_{\text{HB}} = 1.5 \pm 0.2$ kcal/mol per bond (66 ± 9 meV), which is comparable to typical weak HBs. Similar values are obtained for water confined in single-walled carbon nanotubes, with stretching frequency at 3569 and 3640 cm⁻¹, yielding $k \approx 720$ N/m⁴⁹. However, this picture is likely complicated by the interplay between water-water intermolecular HBs and water-carbon π HBs.

At the water-graphene interface, water molecules exhibit a peak around 3600 cm⁻¹, which was assigned to the stretching vibration of the ‘dangling’ O-H dipole pointing towards the graphene film⁵⁰. The reported vibration frequency of $\nu_{\text{OH}} = 3616$ cm⁻¹ for the dangling O-H dipole, using our approach, corresponds to $k = 725.1$ N/m, $E_{\text{HB}} = 1.7 \pm 0.2$ V/nm, $d_{\text{OH}} = 0.975 \pm 0.004$ Å, $p_{\text{H}_2\text{O}} = 2.37 \pm 0.14$ D, and $U_{\text{HB}} = 1.54 \pm 0.20$ kcal/mol per bond (67 ± 9 meV). Our model predicts the electric field exerted by the π electrons on the water O-H dipoles is around 1.7 V/nm. Using only the stretching frequency of confined water, our results directly reproduce key properties of confined water, including HB strength, local E -field, O-H bond length, and dipole moment.

This peak can also be tuned by applying an external electric field in the electric double layer region near graphene surface. In the vicinity of graphene, water O-H dipoles experience an E -field exerted from π electrons of carbon atoms. This interaction can also be considered a π -hydrogen bond (π -HB), which redshifts the stretching frequency of the O-H dipole compared to that of a free water molecule. In the presence of E_{ext} , the interaction is tuned, which can be seen in the shift of the stretching frequency of dangling O-H bond on the graphene surface.

Ref.⁵⁰ reported a sum frequency vibrational spectroscopy (SFVS) study on the water-graphene interface. As an independent validation of our model, we used the data points from Fig. 4b in ref.⁵⁰. The vibration frequency of dangling O-H peak on y-axis is converted to force constant k using harmonic approximation. The interfacial electric field E_s on x-axis corresponds to the E_{ext} in our study. E_{tot} for each point is obtained using Eq. 5 in main text, with E_{HB} given by Eq. 4 (main text) using k at $E_{\text{ext}} = 0$, taken from Fig. 4b in ref.⁵⁰. Since the dangling O-H dipole points towards graphene film, $\cos \vartheta$ in main text Eq (5) is taken as 1. The obtained results match perfectly into our model, as plotted in **Extended Data Fig. 7**.

Dielectric constants of water ice systems

Due to the presence of defects in proton-disordered ices which cause dipole reorientation and, thus, an anomalously large ϵ_r , we chose the proton-ordered ices to study the static ϵ_r . Hence, only atomic and electronic polarization contributions are considered. Ice XI is proton-ordered form of ice Ih, with $\epsilon_r = 2.9$ taken from Fig. 6 in ref.¹⁰¹. The authors cooled down the ordinary ice (ice Ih) and measured ϵ_r at 77 K, where the ice Ih–XI phase transition is expected to occur. The observed small and non-dispersive ϵ_r indicates a proton-ordered form of ordinary ice. The overall static ϵ_r of proton-ordered ice II is around 4.2, measured from Fig. 6 in ref.⁵⁵, although a small increase was observed with frequency (not evaluated). Ice IX is proton-ordered form of ice III. The ϵ_r of ice IX is taken as 4 according to Fig. 3 in ref.¹⁰², where static ϵ_r presented a sharp drop during the ice III – IX phase transition.

We examined the static dielectric constant along [001], [111] and [010] directions for these three phases of ices, respectively, axes direction defined in Refs.¹⁰³⁻¹⁰⁵. The three confined water systems possess 2, 4, and 6 types of non-equivalent O-H dipoles with respect to the assessing axis, with polarizability marked in **Fig. 3d** in main text. Using the neutron diffraction data of O-H bond lengths reported in refs.^{69,72,106} (the bond length of ice III is thermal corrected to 1.005 Å following the approach in Method, ‘Thermal corrections for neutron structural data’) and density reported in refs.^{104,107}, the dielectric constants calculated using Eq. 8 in the main

text, are 3.8 ± 0.5 , 5.9 ± 0.8 and 4.7 ± 0.4 for structure of ice XI, II and IX, respectively. Our results show reasonable agreement with the reported ϵ_r for ice XI, II, and IX, which are 2.9^{101} , 4.2^{55} and 4^{102} .

Acknowledgments

This research was supported by the European Research Council (ERC) under the European Union's Horizon 2020 research and innovation program (Grant Agreement No. 865590) and the Research Council UK [BB/X003736/1]. Q.Y. acknowledges the funding from Royal Society University Research Fellowship URF\R1\221096 and UK Research and Innovation Grant [EP/X017575/1].

Author contributions

A.M. and Q.Y. initiated and supervised the project. Z.W. fabricated devices, performed Raman measurements and analysed the data with the help from I.T. and A.N.G. A.B., M.Y., and F.P. performed DFT calculations. V.K. and A.N.G. helped with FTIR measurements. P.D.N performed scanning near-field microscopy measurements. C.M. carried out the low temperature capacitance measurements. T.T. and K.W. provided hBN crystals. A.M., Z.W., Q.Y., and K.S.N. contributed to writing the paper. All authors discussed the results and commented on the paper.

Data availability

All relevant data are available from the corresponding authors on reasonable request.

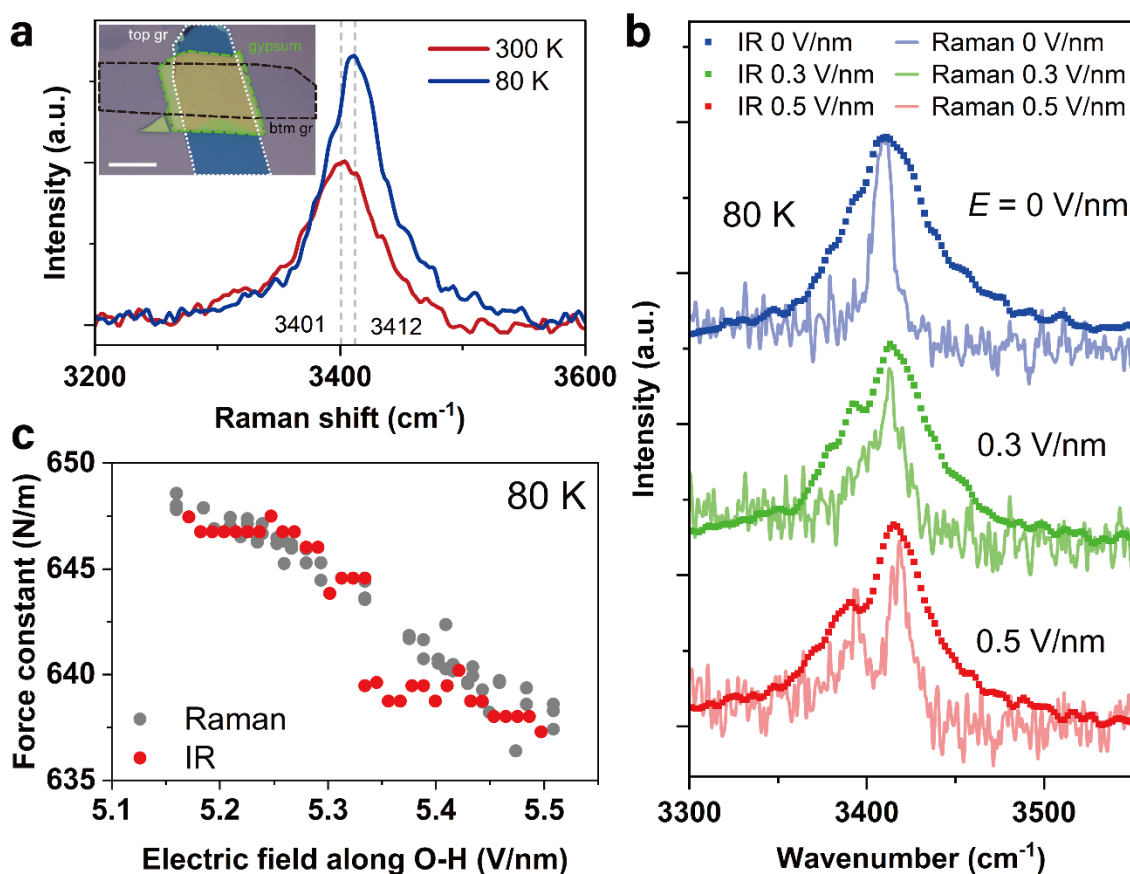
Competing interests

The authors declare no competing interests.

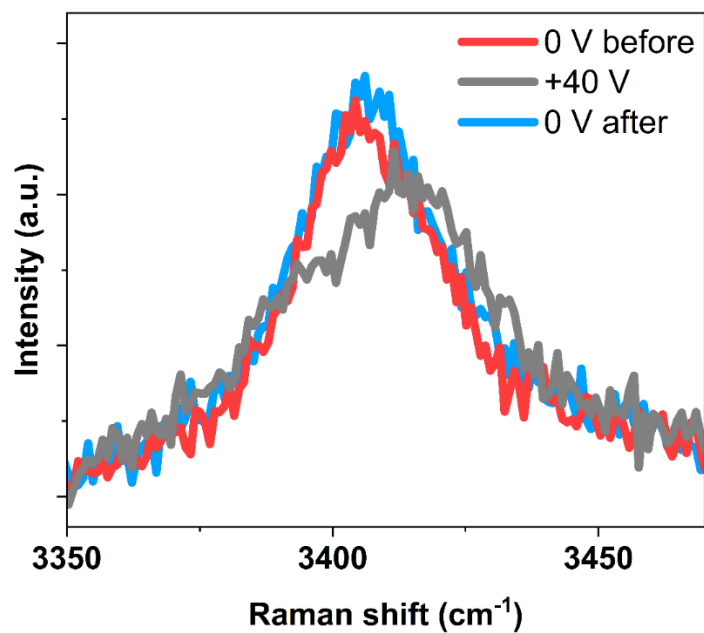
Corresponding authors

Correspondence to Ziwei Wang, Qian Yang or Artem Mishchenko.

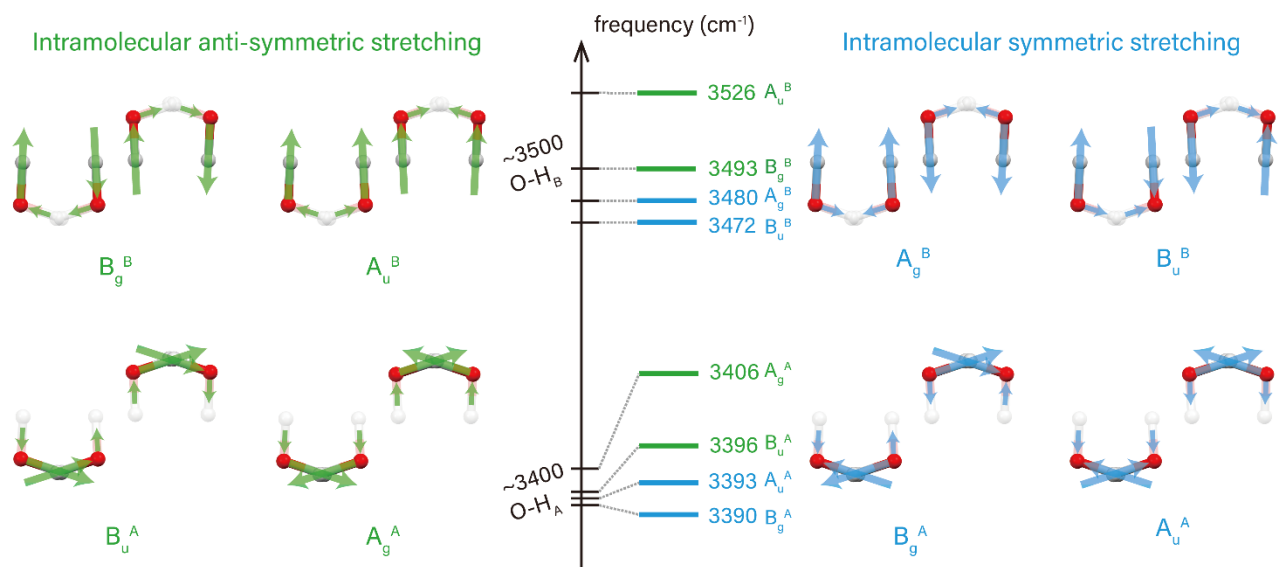
Extended Data



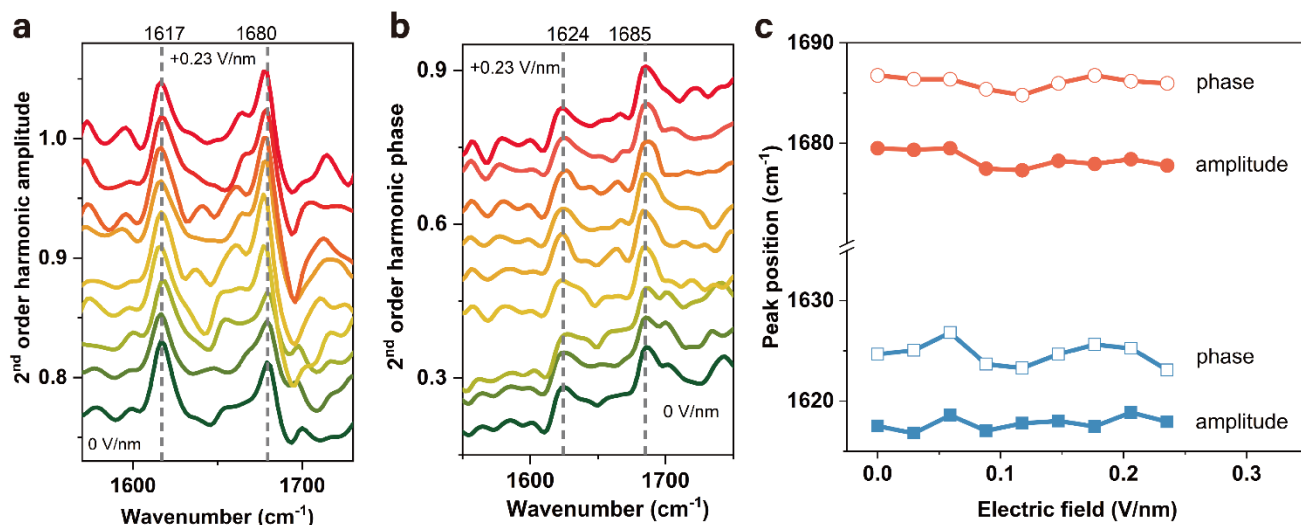
Extended Data Fig. 1: Infrared (IR) study on field-induced peak splitting at low temperature. **a**, Blueshift of water O-H_A stretching peak at 80 K at no external electric field. Inset: optical image of gypsum sample for low-temperature IR measurements. Scale bar 20 μm . **b**, Broadening and splitting of O-H_A stretching peak under external electric field at 80 K (dots). Solid lines are Raman spectra taken from **Fig. 2c** in main text at $E_{\text{ext}} = 0, 0.3,$ and 0.5 V/nm , for comparison. **c**, FTIR peak positions for O-H stretching vibration (red). X-axis plots the total electric field along O-H bond, by adding the local O-H_A field $E_{\text{HB}} = 4.97 \text{ V/nm}$, and taking into account the geometry of H₂O molecules in gypsum. Grey dots correspond to Raman peak positions from **Fig. 3a** in main text.



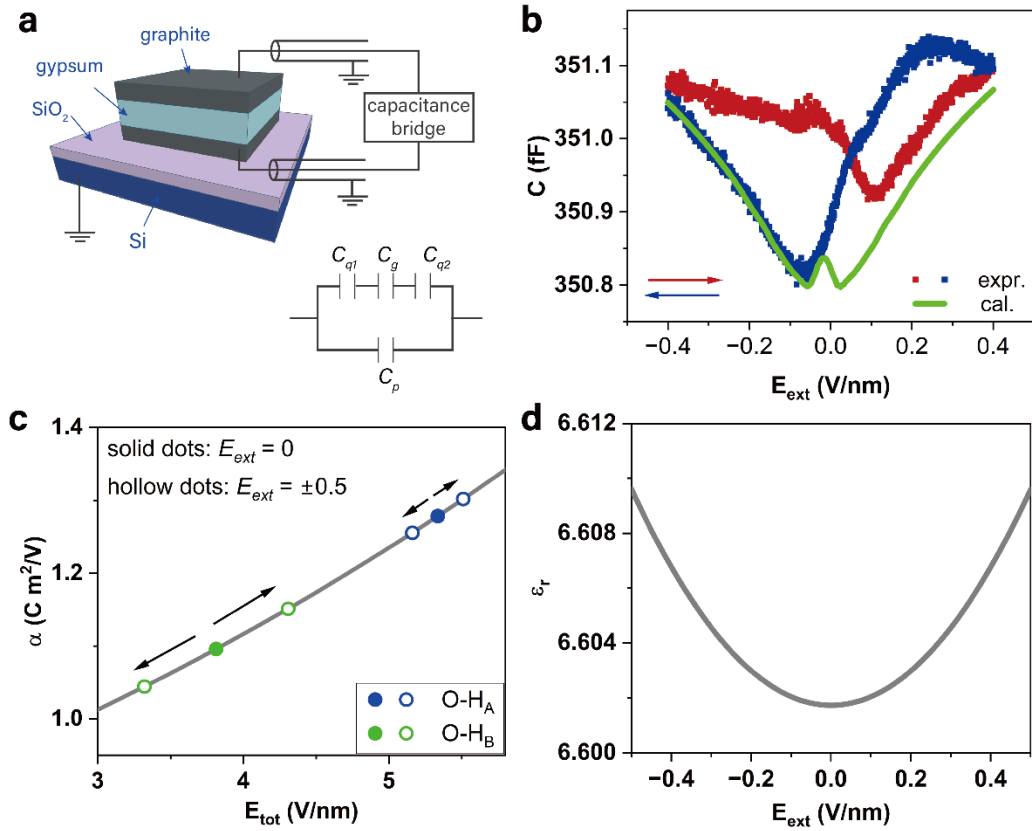
Extended Data Fig. 2: Reversibility of O-H_A stretching peak splitting before and after applying external field. Spectra were taken at 300 K on a graphite/hBN/gypsum/hBN/graphite heterostructure. The electric field at 40 V is 0.31 V/nm, taking into consideration the thickness of gypsum film.



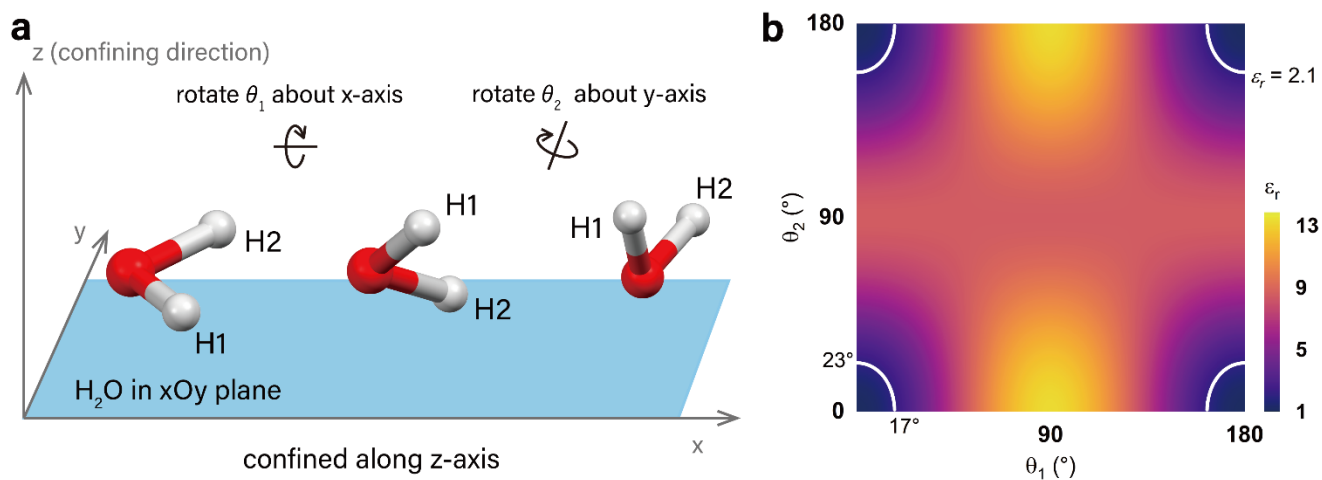
Extended Data Fig. 3: Decoupling of the O-H stretching frequencies in crystalline water of gypsum. Vibration levels of symmetric and antisymmetric stretching are sketched by blue and green solid lines. Blue and green arrows represent the vibration amplitudes of symmetric and antisymmetric stretching, respectively. Longer arrows mean larger vibration amplitudes (the amplitudes are exaggerated for clarity). Symmetric and antisymmetric modes are labelled by A and B, respectively. If the sum of polarizability of the four water molecules changes during vibration, that vibration mode is assigned with a gerade (subscript g) character and is Raman-active. If the sum of dipole moments changes, that vibration mode is assigned with an ungerade (subscript u) character, which is IR-active. Superscripts A and B indicate the mode is from O-H_A or O-H_B vibration.



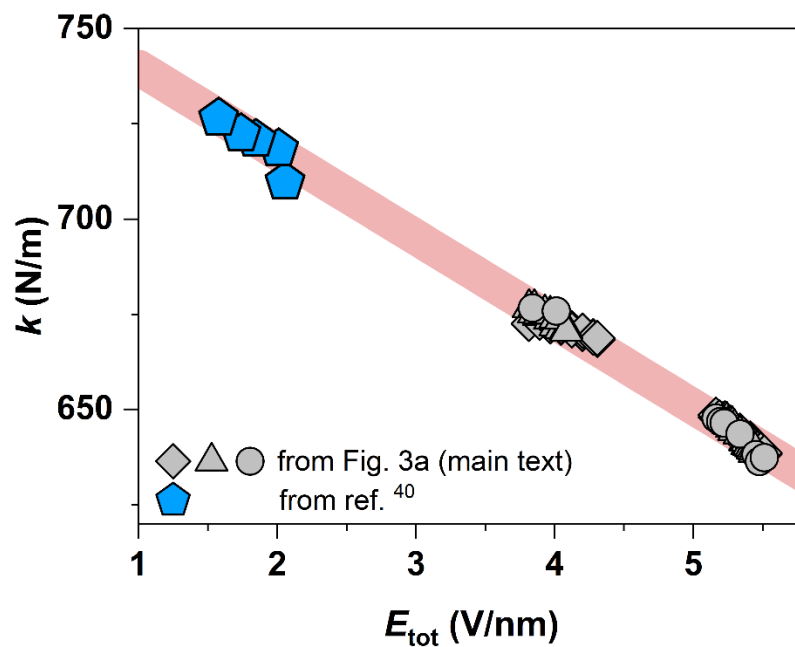
Extended Data Fig. 4: Response of water bending mode to external electric field. **a-b**, nano-FTIR spectra of water bending modes measured using scanning near-field optical microscopy (SNOM). The signal from 2nd harmonic amplitude (**a**) and phase (**b**) are obtained. Two bending vibrations are excited due to the measurement geometry where the incident laser makes an oblique angle to sample stage. **c**, Peak evolution with external electric field along out-of-plane direction. Peak positions extracted from amplitude and phase spectra are plotted as solid and open symbols, respectively. No *E*-field dependence was observed at fields up to 0.23 V/nm.



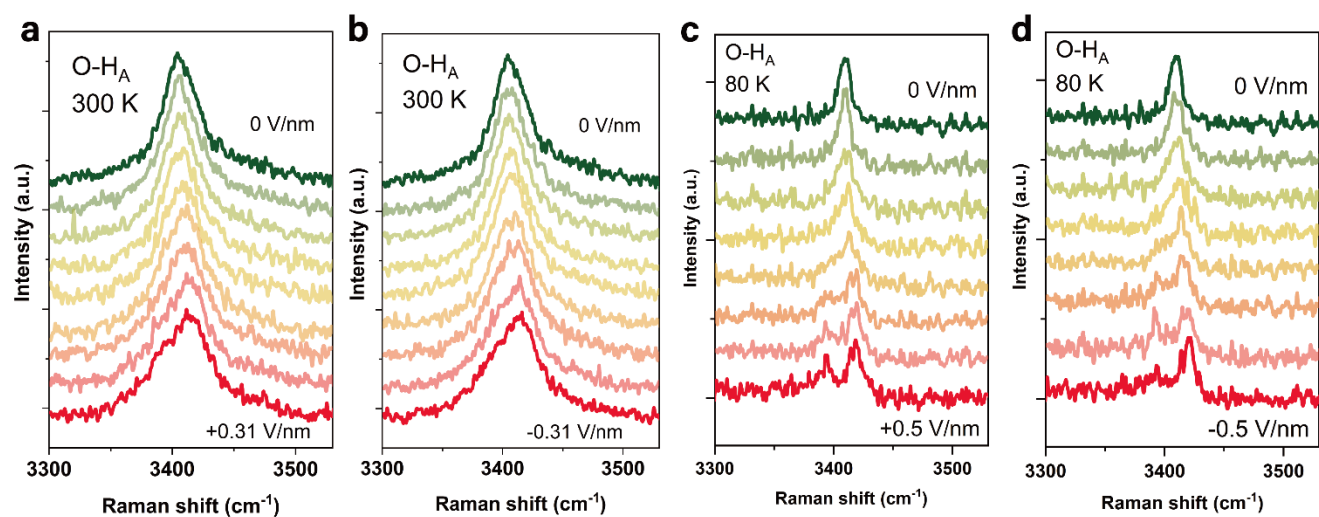
Extended Data Fig. 5: Capacitance measurements and dielectric properties of confined water in gypsum. **a**, Schematic of capacitance measurements. During the measurement, the silicon back gate and the shielding of coaxial cables were grounded to minimize parasitic capacitance contributions. The equivalent circuit of the measurement is sketched, with C_g , C_{q1} (C_{q2}) and C_p being capacitance of gypsum, quantum capacitance of top (bottom) graphite electrode and parasitic capacitance of the setup, respectively. **b**, Capacitance $C(E_{\text{ext}})$ of the graphite/gypsum/graphite heterostructure at 300 K. Arrows denote the sweep direction of E_{ext} . Bias voltage applied between top and bottom graphite electrodes was converted to electric field E_{ext} using the thickness of gypsum determined from AFM measurements (50 nm). Green curve is the calculated total capacitance using Eq. 15. **c**, Calculated polarizability (α) along the O-H bond as a function of total electric field using Eq. 14. Here the total field consists of both internal E_{HB} and the applied E_{ext} . Black arrows denote the modulation of α by E_{ext} ($E_{\text{ext}} = 0$, solid dots; $E_{\text{ext}} = \pm 0.5$ V/nm, hollow dots). **d**, Calculated evolution of ϵ_r in ultra-confined water in gypsum as a function of E_{ext} .



Extended Data Fig. 6: Dielectric constant of confined water. **a**, Schematic of water geometry under confinement. The water molecule is confined along z-direction and has an initial position within xOy plane. The coordinates of O, H1 and H2 are $(0,0,0)$, $(\cos \delta, \sin \delta, 0)$ and $(\cos \delta, -\sin \delta, 0)$. δ is the H-O-H angle. To an arbitrary orientation in 3D space, the water molecule first rotates about x-axis by θ_1 , followed by a second rotation about y-axis by θ_2 . Since rotation about z-axis has no effect on its dielectric properties along confining direction, no z-rotation is considered here. **b**, Dependence of ϵ_r on θ_1 and θ_2 . The white lines mark the orientation which gives experimental $\epsilon_r = 2.1$.⁴⁵



Extended Data Fig. 7: Force constant k vs E_{tot} along O-H bond. Grey symbols are experimental data of this work, same as in the main text Fig. 3a. Blue pentagons are data of water O-H dipoles at water-graphene interface, taken from ref. ⁵⁰. Red line is $k(E)$ relation given by our model (same as in Fig. 3a in the main text).



Extended Data Fig. 8: Raman spectra of O-H_A splitting under E_{ext} . Peak splitting under room temperature (300 K) (a-b) is less pronounced than at 80 K (c-d) due to the thermal broadening effect. Such broadening phenomenon was also observed in other temperature-dependent Raman study of gypsum.⁶⁰

Extended Data Table 1: Raman frequency of O-H stretching and neutron diffraction bond length in different confined-water systems used in Fig. 3b in the main text.

	O-H vibration		O-H bond length (thermal-corrected)	
	Raman shift (cm ⁻¹)	Source	O-H bond length (Å)	Source
Ice Ih	3279 ^a	Ref. ⁶⁸	1.014 ± 0.0011 ^b	Ref. ⁶⁹
Ice II	3194	Ref. ^{70,71}	1.102 ± 0.021 ^b	Ref. ⁷²
Ice VI	3359.5 ^a	Ref. ⁷⁴	1.010 ± 0.028 ^b	Ref. ⁷³
Ice VIII	3427.9	Ref. ⁷⁶	1.010 ± 0.009 ^b	Ref. ⁷⁵
Ice IX	3280.7	Ref. ⁷⁸	0.983 ± 0.004 ^b	Ref. ⁷⁷
Ice XVII	3106.3	Ref. ⁷⁹	1.075 ± 0.007 ^b	Ref. ⁸⁰
	3231.8		1.049 ± 0.004 ^b	
CaSO₄·2H₂O	3406	This work	1.014 ± 0.006 ^b	Ref. ²⁶
	3494		0.995 ± 0.004 ^b	
Li₂SO₄·H₂O	3439	Ref. ⁸²	1.004 ± 0.003	Ref. ⁸¹
	3480		0.997 ± 0.002	
CuSO₄·5H₂O	3360	Ref. ^{83,84}	1.005 ± 0.005	Ref. ⁸⁵
	3477		0.951 ± 0.011	
Ba(ClO₃)₂·H₂O	3547	Ref. ⁸⁷	0.958 ± 0.011	Ref. ⁸⁶
LiClO₄·3H₂O	3553	Ref. ⁸⁹	0.993 ± 0.004	Ref. ⁸⁸
BaCl₂·2H₂O	3303	Ref. ⁹¹	1.077 ± 0.004	Ref. ⁹⁰
	3318		1.072 ± 0.003	
	3352		1.0364 ± 0.0030	
	3456		1.0359 ± 0.0030	

^aDecoupled O-H vibration. ^bMeasured from D₂O water.

References

- 1 Gordon, M. S. & Jensen, J. H. Understanding the Hydrogen Bond Using Quantum Chemistry. *Accounts of Chemical Research* **29**, 536-543 (1996). <https://doi.org:10.1021/ar9600594>
- 2 Steiner, T. The hydrogen bond in the solid state. *Angew Chem Int Ed Engl* **41**, 49-76 (2002). [https://doi.org:10.1002/1521-3773\(20020104\)41:1<48::aid-anie48>3.0.co;2-u](https://doi.org:10.1002/1521-3773(20020104)41:1<48::aid-anie48>3.0.co;2-u)
- 3 Grabowski, S. J. *Hydrogen Bonding - New Insights*. (Springer Dordrecht, 2006).
- 4 Li, X.-Z., Walker, B. & Michaelides, A. Quantum nature of the hydrogen bond. *Proceedings of the National Academy of Sciences* **108**, 6369-6373 (2011). <https://doi.org:10.1073/pnas.1016653108>
- 5 Herschlag, D. & Pinney, M. M. Hydrogen Bonds: Simple after All? *Biochemistry* **57**, 3338-3352 (2018). <https://doi.org:10.1021/acs.biochem.8b00217>
- 6 Dereka, B. *et al.* Crossover from hydrogen to chemical bonding. *Science* **371**, 160-164 (2021). <https://doi.org:10.1126/science.abe1951>
- 7 Arunan, E. *et al.* Definition of the hydrogen bond (IUPAC Recommendations 2011). *Pure Appl. Chem.* **83**, 1637-1641 (2011). <https://doi.org:10.1351/pac-rec-10-01-02>
- 8 Arunan, E. *et al.* Defining the hydrogen bond: An account (IUPAC Technical Report). *Pure Appl. Chem.* **83**, 1619-1636 (2011). <https://doi.org:10.1351/pac-rep-10-01-01>
- 9 Ceriotti, M., Cuny, J., Parrinello, M. & Manolopoulos, D. E. Nuclear quantum effects and hydrogen bond fluctuations in water. *Proc Natl Acad Sci U S A* **110**, 15591-15596 (2013). <https://doi.org:10.1073/pnas.1308560110>
- 10 Van Hoozen, B. L., Jr. & Petersen, P. B. Vibrational tug-of-war: The pK(A) dependence of the broad vibrational features of strongly hydrogen-bonded carboxylic acids. *J Chem Phys* **148**, 134309 (2018). <https://doi.org:10.1063/1.5026675>
- 11 Cleland, W. W. & Kreevoy, M. M. Low-barrier hydrogen bonds and enzymic catalysis. *Science* **264**, 1887-1890 (1994). <https://doi.org:10.1126/science.8009219>
- 12 Carrasco, J., Hodgson, A. & Michaelides, A. A molecular perspective of water at metal interfaces. *Nat Mater* **11**, 667-674 (2012). <https://doi.org:10.1038/nmat3354>
- 13 Martin, L. W. & Rappe, A. M. Thin-film ferroelectric materials and their applications. *Nature Reviews Materials* **2**, 1-14 (2016). <https://doi.org:10.1038/natrevmats.2016.87>
- 14 Zhang, Z., Ye, Y., Xiang, S. & Chen, B. Exploring Multifunctional Hydrogen-Bonded Organic Framework Materials. *Acc Chem Res* **55**, 3752-3766 (2022). <https://doi.org:10.1021/acs.accounts.2c00686>
- 15 Shi, B. *et al.* Short hydrogen-bond network confined on COF surfaces enables ultrahigh proton conductivity. *Nat Commun* **13**, 6666 (2022). <https://doi.org:10.1038/s41467-022-33868-8>
- 16 Lin, Z. J., Mahammed, S. A. R., Liu, T. F. & Cao, R. Multifunctional Porous Hydrogen-Bonded Organic Frameworks: Current Status and Future Perspectives. *ACS Cent Sci* **8**, 1589-1608 (2022). <https://doi.org:10.1021/acscentsci.2c01196>
- 17 Pal, S. C., Mukherjee, D., Sahoo, R., Mondal, S. & Das, M. C. Proton-Conducting Hydrogen-Bonded Organic Frameworks. *ACS Energy Letters* **6**, 4431-4453 (2021). <https://doi.org:10.1021/acseenergylett.1c02045>
- 18 Li, P., Ryder, M. R. & Stoddart, J. F. Hydrogen-Bonded Organic Frameworks: A Rising Class of Porous Molecular Materials. *Accounts of Materials Research* **1**, 77-87 (2020). <https://doi.org:10.1021/accountsmr.0c00019>
- 19 Pauling, L. The shared-electron chemical bond. *Proceedings of the national academy of sciences* **14**, 359-362 (1928).
- 20 Yamabe, S. & Morokuma, K. Molecular orbital studies of hydrogen bonds. IX. Electron distribution analysis. *Journal of the American Chemical Society* **97**, 4458-4465 (1975).
- 21 Paoloni, L. Nature of the Hydrogen Bond. *The Journal of Chemical Physics* **30**, 1045-1058 (1959).
- 22 Kolesov, B. A. Hydrogen bonds: Raman spectroscopic study. *International journal of molecular sciences* **22**, 5380 (2021).
- 23 Hush, N. S. & Williams, M. L. Carbon monoxide bond length, force constant and infrared intensity variations in strong electric fields: Valence-shell calculations, with applications to properties of adsorbed and complexed CO. *Journal of Molecular Spectroscopy* **50**, 349-368 (1974). [https://doi.org:10.1016/0022-2852\(74\)90241-0](https://doi.org:10.1016/0022-2852(74)90241-0)
- 24 Cole, W. F. & Lancucki, C. J. Symmetry of SO₄ Ion in Gypsum. *Nature Physical Science* **238**, 95-96 (1972). <https://doi.org:10.1038/physci238095a0>
- 25 Cole, W. F. & Lancucki, C. J. Hydrogen Bonding in Gypsum. *Nature Physical Science* **242**, 104-105 (1973). <https://doi.org:10.1038/physci242104b0>
- 26 Schofield, P. F., Knight, K. S. & Stretton, I. C. Thermal expansion of gypsum investigated by neutron powder diffraction. *American Mineralogist* **81**, 847-851 (1996).
- 27 Frisenda, R. *et al.* Recent progress in the assembly of nanodevices and van der Waals heterostructures by deterministic placement of 2D materials. *Chemical Society Reviews* **47**, 53-68 (2018).

- 28 Couty, R., Velde, B. & Besson, J. M. Raman spectra of gypsum under pressure. *Physics and Chemistry of Minerals* **10**, 89-93 (1983). <https://doi.org:10.1007/bf00309590>
- 29 Seki, T. *et al.* The Bending Mode of Water: A Powerful Probe for Hydrogen Bond Structure of Aqueous Systems. *J Phys Chem Lett* **11**, 8459-8469 (2020). <https://doi.org:10.1021/acs.jpcelett.0c01259>
- 30 Furtenbacher, T., Tóbiás, R., Tennyson, J., Polyansky, O. L. & Császár, A. G. W2020: A Database of Validated Rovibrational Experimental Transitions and Empirical Energy Levels of H₂O. *Journal of Physical and Chemical Reference Data* **49** (2020). <https://doi.org:10.1063/5.0008253>
- 31 Hoy, A. R. & Bunker, P. R. A precise solution of the rotation bending Schrödinger equation for a triatomic molecule with application to the water molecule. *Journal of Molecular Spectroscopy* **74**, 1-8 (1979). [https://doi.org:10.1016/0022-2852\(79\)90019-5](https://doi.org:10.1016/0022-2852(79)90019-5)
- 32 Csaszar, A. G. *et al.* On equilibrium structures of the water molecule. *J Chem Phys* **122**, 214305 (2005). <https://doi.org:10.1063/1.1924506>
- 33 Beers, Y. & Klein, G. P. The Stark Splitting of Millimeter Wave Transitions of Water. *J Res Natl Bur Stand A Phys Chem* **76A**, 521-528 (1972). <https://doi.org:10.6028/jres.076A.048>
- 34 Clough, S. A., Beers, Y., Klein, G. P. & Rothman, L. S. Dipole moment of water from Stark measurements of H₂O, HDO, and D₂O. *The Journal of Chemical Physics* **59**, 2254-2259 (1973).
- 35 Lovas, F. J. Microwave spectral tables II. Triatomic molecules. *Journal of Physical and Chemical Reference Data* **7**, 1445-1750 (1978). <https://doi.org:10.1063/1.555588>
- 36 Lodi, L. *et al.* A new ab initio ground-state dipole moment surface for the water molecule. *J Chem Phys* **128**, 044304 (2008). <https://doi.org:10.1063/1.2817606>
- 37 Badyal, Y. *et al.* Electron distribution in water. *The Journal of Chemical Physics* **112**, 9206-9208 (2000).
- 38 Batista, E. R., Xantheas, S. S. & Jónsson, H. Molecular multipole moments of water molecules in ice Ih. *The Journal of chemical physics* **109**, 4546-4551 (1998).
- 39 Carey, D. M. & Korenowski, G. M. Measurement of the Raman spectrum of liquid water. *The Journal of chemical physics* **108**, 2669-2675 (1998).
- 40 Walrafen, G. Raman spectral studies of the effects of temperature on water structure. *The Journal of Chemical Physics* **47**, 114-126 (1967).
- 41 Whalley, E. Energies of the phases of ice at zero temperature and pressure. *The Journal of chemical physics* **81**, 4087-4092 (1984).
- 42 Nanayakkara, S., Tao, Y. & Kraka, E. Capturing individual hydrogen bond strengths in ices via periodic local vibrational mode theory: Beyond the lattice energy picture. *Journal of Chemical Theory and Computation* **18**, 562-579 (2021).
- 43 Suresh, S. & Naik, V. Hydrogen bond thermodynamic properties of water from dielectric constant data. *The Journal of Chemical Physics* **113**, 9727-9732 (2000).
- 44 López-Buendía, A. M., García-Baños, B., Urquiola, M. M., Catalá-Civera, J. M. & Penaranda-Foix, F. L. Evidence of a new phase in gypsum-anhydrite transformations under microwave heating by in situ dielectric analysis and Raman spectroscopy. *Physical Chemistry Chemical Physics* **22**, 27713-27723 (2020).
- 45 Fumagalli, L. *et al.* Anomalously low dielectric constant of confined water. *Science* **360**, 1339-1342 (2018).
- 46 Michaelides, A. *et al.* Origin of dielectric polarization suppression in confined water from first principles. (2023).
- 47 Bocquet, L. Nanofluidics coming of age. *Nature Materials* **19**, 254-256 (2020). <https://doi.org:10.1038/s41563-020-0625-8>
- 48 Shugai, A. *et al.* Infrared spectroscopy of an endohedral water in fullerene. *J Chem Phys* **154**, 124311 (2021). <https://doi.org:10.1063/5.0047350>
- 49 Dalla Bernardina, S. *et al.* Water in carbon nanotubes: the peculiar hydrogen bond network revealed by infrared spectroscopy. *Journal of the American Chemical Society* **138**, 10437-10443 (2016).
- 50 Xu, Y., Ma, Y.-B., Gu, F., Yang, S.-S. & Tian, C.-S. Structure evolution at the gate-tunable suspended graphene-water interface. *Nature* **621**, 506-510 (2023).
- 51 Caillol, J. Asymptotic behavior of the pair-correlation function of a polar liquid. *The Journal of chemical physics* **96**, 7039-7053 (1992).
- 52 Sharma, M., Resta, R. & Car, R. Dipolar correlations and the dielectric permittivity of water. *Physical review letters* **98**, 247401 (2007).
- 53 Olivieri, J.-F., Hynes, J. T. & Laage, D. Confined water's dielectric constant reduction is due to the surrounding low dielectric media and not to interfacial molecular ordering. *The Journal of Physical Chemistry Letters* **12**, 4319-4326 (2021).
- 54 Gränicher, H., Jaccard, C., Scherrer, P. & Steinemann, A. Dielectric relaxation and the electrical conductivity of ice crystals. *Discussions of the faraday society* **23**, 50-62 (1957).
- 55 Wilson, G., Chan, R., Davidson, D. & Whalley, E. Dielectric properties of ices II, III, V, and VI. *The journal of chemical physics* **43**, 2384-2391 (1965).

- 56 Bramwell, S. T. Ferroelectric ice. *Nature* **397**, 212-213 (1999). <https://doi.org/10.1038/16594>
- 57 Keutsch, F. N. & Saykally, R. J. Water clusters: untangling the mysteries of the liquid, one molecule at a time. *Proc Natl Acad Sci U S A* **98**, 10533-10540 (2001). <https://doi.org/10.1073/pnas.191266498>
- 58 Castellanos-Gomez, A. *et al.* Deterministic transfer of two-dimensional materials by all-dry viscoelastic stamping. *2D Materials* **1**, 011002 (2014).
- 59 Pizzocchero, F. *et al.* The hot pick-up technique for batch assembly of van der Waals heterostructures. *Nat Commun* **7**, 11894 (2016). <https://doi.org/10.1038/ncomms11894>
- 60 Chio, C. H., Sharma, S. K. & Muenow, D. W. Micro-Raman studies of gypsum in the temperature range between 9 K and 373 K. *American Mineralogist* **89**, 390-395 (2004).
- 61 Flaud, J. M. & Camy-Peyret, C. The interacting states (020), (100), and (001) of H₂16O. *Journal of Molecular Spectroscopy* **51**, 142-150 (1974). [https://doi.org/10.1016/0022-2852\(74\)90177-5](https://doi.org/10.1016/0022-2852(74)90177-5)
- 62 Flaud, J. M. & Camy-Peyret, C. Vibration-rotation intensities in H₂O-type molecules application to the 2v₂, v₁, and v₃ bands of H₂16O. *Journal of Molecular Spectroscopy* **55**, 278-310 (1975). [https://doi.org/10.1016/0022-2852\(75\)90270-2](https://doi.org/10.1016/0022-2852(75)90270-2)
- 63 Murphy, W. F. The rovibrational Raman spectrum of water vapour v₁ and v₃. *Molecular Physics* **36**, 727-732 (1978). <https://doi.org/10.1080/00268977800101881>
- 64 Rahn, L. A. & Greenhalgh, D. A. High-resolution inverse Raman spectroscopy of the v₁ band of water vapor. *Journal of Molecular Spectroscopy* **119**, 11-21 (1986). [https://doi.org/10.1016/0022-2852\(86\)90197-9](https://doi.org/10.1016/0022-2852(86)90197-9)
- 65 Tennyson, J. *et al.* IUPAC critical evaluation of the rotational–vibrational spectra of water vapor. Part II. *Journal of Quantitative Spectroscopy and Radiative Transfer* **111**, 2160-2184 (2010). <https://doi.org/10.1016/j.jqsrt.2010.06.012>
- 66 Busing, W. R. & Levy, H. A. The effect of thermal motion on the estimation of bond lengths from diffraction measurements. *Acta Crystallographica* **17**, 142-146 (1964).
- 67 Soper, A. K. & Benmore, C. J. Quantum Differences between Heavy and Light Water. *Physical Review Letters* **101**, 065502 (2008). <https://doi.org/10.1103/PhysRevLett.101.065502>
- 68 Scherer, J. R. & Snyder, R. G. Raman intensities of single crystal ice I_h. *The Journal of Chemical Physics* **67**, 4794-4811 (1977).
- 69 Kuhs, W. F. & Lehmann, M. S. The structure of the ice I_h by neutron diffraction. *The Journal of Physical Chemistry* **87**, 4312-4313 (1983). <https://doi.org/10.1021/j100244a063>
- 70 Taylor, M. & Whalley, E. Raman spectra of ices I_h, I_c, II, III, and V. *The Journal of Chemical Physics* **40**, 1660-1664 (1964).
- 71 Minceva-Sukarova, B., Sherman, W. & Wilkinson, G. The Raman spectra of ice (I_h, II, III, V, VI and IX) as functions of pressure and temperature. *Journal of Physics C: Solid State Physics* **17**, 5833 (1984).
- 72 Kamb, B., Hamilton, W. C., LaPlaca, S. J. & Prakash, A. Ordered proton configuration in ice II, from single-crystal neutron diffraction. *The Journal of Chemical Physics* **55**, 1934-1945 (1971).
- 73 Kuhs, W. F., Finney, J. L., Vettier, C. & Bliss, D. V. Structure and hydrogen ordering in ices VI, VII, and VIII by neutron powder diffraction. *The Journal of Chemical Physics* **81**, 3612-3623 (1984). <https://doi.org/10.1063/1.448109>
- 74 Thoeny, A. V., Parrichini, I. S., Gasser, T. M. & Loerting, T. Raman spectroscopy study of the slow order-order transformation of deuterium atoms: Ice XIX decay and ice XV formation. *J Chem Phys* **156**, 154507 (2022). <https://doi.org/10.1063/5.0087592>
- 75 Jorgensen, J. D., Beyerlein, R., Watanabe, N. & Worlton, T. Structure of D₂O ice VIII from insitu powder neutron diffraction. *The Journal of chemical physics* **81**, 3211-3214 (1984).
- 76 Wong, P. & Whalley, E. Raman spectrum of ice VIII. *The Journal of Chemical Physics* **64**, 2359-2366 (1976).
- 77 La Placa, S. J., Hamilton, W. C., Kamb, B. & Prakash, A. On a nearly proton-ordered structure for ice IX. *The Journal of Chemical Physics* **58**, 567-580 (1973).
- 78 Bertie, J. E. & Francis, B. F. Raman spectra of the O–H and O–D stretching vibrations of ices II and IX to 25 K at atmospheric pressure. *The Journal of Chemical Physics* **72**, 2213-2221 (1980).
- 79 Del Rosso, L. *et al.* Cubic ice I_c without stacking defects obtained from ice XVII. *Nature Mater.* **19**, 663-668 (2020).
- 80 del Rosso, L. *et al.* Refined structure of metastable ice XVII from neutron diffraction measurements. *The Journal of Physical Chemistry C* **120**, 26955-26959 (2016).
- 81 Lundgren, J. O., Kvik, Å., Karppinen, M., Liminga, R. & Abrahams, S. Neutron diffraction structural study of pyroelectric Li₂SO₄·H₂O at 293, 80, and 20 K. *The Journal of chemical physics* **80**, 423-430 (1984).
- 82 Canterford, R. & Ninio, F. Raman study of some water modes in lithium sulphate monohydrate. *Solid State Commun.* **15**, 1451-1452 (1974).
- 83 Liu, D. & Ullman, F. Raman spectrum of CuSO₄·5H₂O single crystal. *Journal of Raman spectroscopy* **22**, 525-528 (1991).

- 84 Berger, J. Infrared and Raman spectra of $\text{CuSO}_4 \cdot 5\text{H}_2\text{O}$; $\text{CuSO}_4 \cdot 5\text{D}_2\text{O}$; and $\text{CuSeO}_4 \cdot 5\text{H}_2\text{O}$. *Journal of Raman Spectroscopy* **5**, 103-114 (1976).
- 85 Bacon, G. & Titterton, D. Neutron-diffraction studies of $\text{CuSO}_4 \cdot 5\text{H}_2\text{O}$ and $\text{CuSO}_4 \cdot 5\text{D}_2\text{O}$. *Zeitschrift für Kristallographie-Crystalline Materials* **141**, 330-341 (1975).
- 86 Sikka, S., Momin, S., Rajagopal, H. & Chidambaram, R. Neutron-diffraction refinement of the crystal structure of barium chlorate monohydrate $\text{Ba}(\text{ClO}_3)_2 \cdot \text{H}_2\text{O}$. *The Journal of Chemical Physics* **48**, 1883-1889 (1968).
- 87 Bertie, J. E., Heyns, A. M. & Oehler, O. The Infrared and Raman Spectra of Powdered and Single-Crystal Barium Chlorate Monohydrate and-deuterate. *Canadian Journal of Chemistry* **51**, 2275-2289 (1973).
- 88 Lundgren, J.-O., Liminga, R. & Tellgren, R. Neutron diffraction refinement of pyroelectric lithium perchlorate trihydrate. *Acta Crystallographica Section B: Structural Crystallography and Crystal Chemistry* **38**, 15-20 (1982).
- 89 Zhang, Y.-H. & Chan, C. K. Observations of water monomers in supersaturated NaClO_4 , LiClO_4 , and $\text{Mg}(\text{ClO}_4)_2$ droplets using Raman spectroscopy. *The Journal of Physical Chemistry A* **107**, 5956-5962 (2003).
- 90 Padmanabhan, V., Busing, W. & Levy, H. A. Barium chloride dihydrate by neutron diffraction. *Acta Crystallographica Section B: Structural Crystallography and Crystal Chemistry* **34**, 2290-2292 (1978).
- 91 Lutz, H., Pobitschka, W., Frischemeier, B. & Becker, R.-A. Lattice Vibration Spectra. XX. Infrared and Raman Spectra of $\text{BaCl}_2 \cdot 2\text{H}_2\text{O}$ and $\text{BaCl}_2 \cdot 2\text{D}_2\text{O}$. *Applied Spectroscopy* **32**, 541-547 (1978).
- 92 Soper, A. Joint structure refinement of x-ray and neutron diffraction data on disordered materials: application to liquid water. *Journal of Physics: Condensed Matter* **19**, 335206 (2007).
- 93 Mullan, C. *et al.* Mixing of moiré-surface and bulk states in graphite. *Nature* **620**, 756-761 (2023).
- 94 Robie, R. A. & Bethke, P. M. Molar volumes and densities of minerals. *Unites States Department of the Interior Geological Survey*, 4-21 (1962).
- 95 Lin, Y., Shiomi, J., Maruyama, S. & Amberg, G. Dielectric relaxation of water inside a single-walled carbon nanotube. *Phys. Rev. B* **80**, 045419 (2009).
- 96 Loche, P., Ayaz, C., Schlaich, A., Uematsu, Y. & Netz, R. R. Giant axial dielectric response in water-filled nanotubes and effective electrostatic ion-ion interactions from a tensorial dielectric model. *The Journal of Physical Chemistry B* **123**, 10850-10857 (2019).
- 97 Renou, R., Szymczyk, A. & Ghoufi, A. Tunable dielectric constant of water at the nanoscale. *Physical Review E* **91**, 032411 (2015).
- 98 Sarhangi, S. M., Waskasi, M. M., Hashemianzadeh, S. M. & Matyushov, D. V. Effective dielectric constant of water at the interface with charged C60 fullerenes. *The Journal of Physical Chemistry B* **123**, 3135-3143 (2019).
- 99 Meier, B. *et al.* Electrical detection of ortho-para conversion in fullerene-encapsulated water. *Nature Communications* **6**, 8112 (2015).
- 100 Debye, P. Einige resultate einer kinetischen theorie der isolatoren. *Physik Z.* **13**, 97 (1912).
- 101 Shimizu, N. & Muramoto, Y. Natural materials adopted for electrical and electronic materials. *IEEJ Transactions on Fundamentals and Materials* **127**, 429-432 (2007).
- 102 Whalley, E., Heath, J. & Davidson, D. Ice IX: an antiferroelectric phase related to ice III. *The Journal of Chemical Physics* **48**, 2362-2370 (1968).
- 103 Bernal, J. D. & Fowler, R. H. A theory of water and ionic solution, with particular reference to hydrogen and hydroxyl ions. *The Journal of Chemical Physics* **1**, 515-548 (1933).
- 104 Kamb, B. Ice. ii. a proton-ordered form of ice. *Acta crystallographica* **17**, 1437-1449 (1964).
- 105 Kamb, B. & Prakash, A. Structure of ice III. *Acta Crystallographica Section B: Structural Crystallography and Crystal Chemistry* **24**, 1317-1327 (1968).
- 106 Londono, J. D., Kuhs, W. F. & Finney, J. L. Neutron diffraction studies of ices III and IX on under-pressure and recovered samples. *The Journal of Chemical Physics* **98**, 4878-4888 (1993). <https://doi.org/10.1063/1.464942>
- 107 Bridgman, P. W. *Water, in the liquid and five solid forms, under pressure.* (American Academy of Arts and Sciences, Cambridge, MA, 1913).